

## Revisit the Oort constants measurement from *Gaia DR2* observations and simulations

SHUFAN XIA,<sup>1</sup> KARENS MASTERS,<sup>1</sup> AND ZHAO-YU LI<sup>2</sup>

<sup>1</sup>*Haverford College, Department of Physics and Astronomy*

<sup>2</sup>*Shanghai Jiaotong University, Department of Astronomy*

### ABSTRACT

The Oort constants are a set of empirical constants which can be used to reveal rotational kinematics of the Milky Way (MW) disk in the solar neighborhood. The orbital properties of the Sun can be estimated from the Oort constants. They also prove the radial profiles of the circular velocity in the MW and the mass density. An accurate determination of this set of constants helps us derive the MW rotation curve in the Sun’s immediate neighborhood and to understand the general kinematic properties of the MW disk. *Gaia* provides massive and exquisite data on parallax and proper motion for billions of stars in the Milky Way. These data make it possible to determine the Oort constants in the solar vicinity with unprecedented accuracy. In this thesis, combining test particle simulation and the recent *Gaia* DR2 data, we examine the influence of different sampling criteria of the stellar distance and latitude ranges in Galactic Coordinates deriving the Oort constant. From the simulation, it seems that it is necessary to limit the distance within 1kpc and latitude range  $|b| < 20^\circ$  to achieve a good fit based on the longitudinal profile of  $\mu_l$  and  $v_{los}$ . The longitudinal profile of  $\mu_l$  is generally not as good as the other two kinematic tracers. However, reasonable Oort constants could be estimated if the latitude range is limited to  $30^\circ < |b| < 50^\circ$ . We apply the sample selection criteria from previous literature on using proper motion and line-of-sight velocity data from *Gaia* DR2 and compare the result with the criteria determined from our test particle simulations. We found  $A = 15.52 \pm 0.22$ ,  $B = -13.33 \pm 0.17$ ,  $C = -1.88 \pm 0.08$ , and  $K = -1.86 \pm 0.19$  km/s/kpc from *Gaia* DR2 observational data, which are consistent with previous works.

### 1. INTRODUCTION

The simplest model of the Milky Way (MW) proposes that our galaxy is a flat circular disk, and stars move on perfectly circular orbits around the galactic center (GC).

Corresponding author: Shufan Xia  
[sxia1@haverford.edu](mailto:sxia1@haverford.edu)

However, the structure and the dynamics of our galaxy is much more complicated. Our galaxy is a barred-spiral galaxy with non-axisymmetric and time-dependent perturbation to its potential. Due to perturbation in the MW potential, all stars have non-circular components to their orbital energy, so they move in "rosette" and non-closed orbits (Binney & Merrifield 1998; Bovy 2017). The rotational kinematics of the MW are, therefore, complicated to quantify. The Oort constants are a set of empirically derived kinematic parameters notated typically with  $A$ ,  $B$ ,  $C$ , and  $K$  that characterize the local rotation properties in the Milky Way. They have been used extensively in the study of the rotational kinematics of our galaxy.

To help us keep track of the different velocities in the following discussion, here I list the notation for velocity components used throughout this paper. In Galactocentric cylindrical coordinate,  $v_{circ}$  or  $v_\phi$  is the circular velocity about the Galactic Center(GC);  $v_r$  is the radial velocity with respect to the GC;  $v_z$  is vertical velocity away from the Milky Way (MW) plane. In Galactic coordinates (discussed further in Section 1.2),  $v_{los}$  is the line of sight velocity as seen from the Sun;  $v_l$  is the velocity component perpendicular to the line of sight in the Galactic longitude ( $l$ ) direction; and  $v_b$  represents the velocity component perpendicular to the line of sight in the Galactic latitude ( $b$ ) direction.

### 1.1. *The Milky Way Rotation Curve*

The rotation curves of galaxies are used to illustrate the dependency of circular rotational velocity,  $v_\phi$ , about the galactic center on distance from the center. Pioneered by Vera Rubin, galactic rotation curves have been studied as the evidence of Dark Matters. For our Milky Way, this rotation curve is flat but slightly declining from the radius of the Sun and beyond. The mass components and their distributions in our Galaxy have been derived from this curve. Fig. 1 shows a recent measurement of the MW rotation curve (Eilers et al. 2019). The overall rotation curve comes from adding up the contributions from different components of mass - the central bulge, stellar disc, other stellar components and the dark matter halo (Olling & Merrifield 1998).

Using Newtonian Mechanics, we can connect velocity, potential, and mass distribution (Binney & Merrifield 1998); therefore, stellar kinematics is a mass probe. The application of measuring rotation curves are multiple: they can be used to study kinematics, evolutionary histories of galaxies, and departures from Keplerian for the possible existence of the dark matter (Sofue & Rubin 2001). However, measuring the Milky Way rotation curve is challenging because of the observation constraints caused by our location in the Milky Way. We are in one of the spiral arms of the Galaxy, the Orion Arm(Binney & Merrifield 1998). This means that our line of sight is blocked by the dust in the disk, so we can not observe stars far from the Sun. The fact that we are co-moving with the Galaxy also makes it challenging to determine

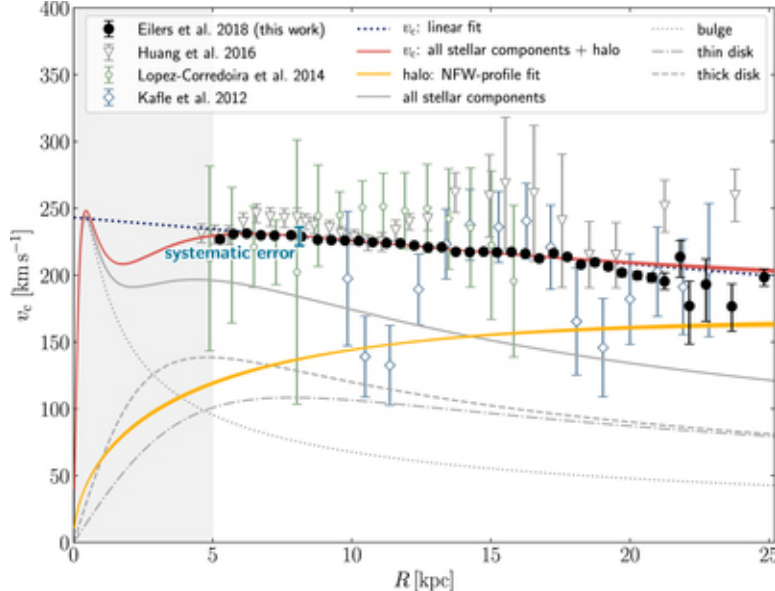


**Figure 1:** Recent measurements of the circular velocity curve of the Milky Way. The red curve is an approximate overall rotation curve (Eilers et al. 2019).

relative motion. Therefore, measuring the whole rotation curve remains a challenging task.

Various tracers and methods have been used to track the rotation curve. Determining the tracers' distances is always difficult for astronomers because the extinction from interstellar medium adds challenge to accurate measurement. For the inner region within the Sun, the MW rotation curve has been determined via the tangent-point method which uses the line of sight velocity along certain observational direction measured from the shifts in the emission lines of the gas clouds in CO, H I, and H II regions under Doppler's effect (Levine et al. 2008). Based on geometric and trigonometric derivations, this method is able determine distances and rotation velocity just from the terminal radial velocities of gas clouds in a fixed direction with respect to the observer. The maximum line of sight velocity in a fixed observational direction corresponds to the circular velocity at the radius of the tangent point from the Galactic center. By sweeping through many different observational angles, we can map out the function of circular velocity against the radius. The rotation curve of the outer region beyond the Sun has been measured by other tracers, such as classical Cepheid (Joy 1939; Metzger et al. 1998; Mróz et al. 2019), RR Lyrae stars (Wegg et al. 2019), and luminous red giant stars (Eilers et al. 2019). Both classical Cepheids and RR lyrae stars are better for determining rotation curve because they are intrinsically bright and their distance-period relationship makes distance measurement more reliable. (Metzger et al. 1998)

### 1.2. Oort constants

While many methods to obtain constraint on the rotation curve require difficult observational measurements across a very large space, we can use the Oort constants

to describe local rotational properties. The Oort constants  $A$  and  $B$  (which are explained more in section 1.3 below) tell us the local rotational velocity around the Galactic Center and the local slope of the rotational curve (Binney & Merrifield 1998). The power of the Oort constants is that they are local parameters, but they enable us to test against different rotational models from their predicted rotation curves. This work looks at the Oort constants in the vicinity of our Sun. An accurate measurement of the Oort constants in this region will potentially help us determine the local rotation curve, Galactic radius, and rotational velocity of the Sun (Olling & Merrifield 1998), as well as the eccentricity of the solar orbit (Kuijken & Tremaine 1994; Metzger et al. 1998).

To study the local rotation near the Sun and the Oort constants requires an understanding of Galactic coordinates. They are in a spherical coordinate system, with the Sun at its center and its plane parallel to the Milky Way midplane. Galactic longitude  $l$  is the counter-clockwise azimuthal angle measured from the Galactic center at  $l = 0$ , and the Galactic longitude,  $b$ , is the elevation angle (See Fig. 2). However, because the Sun actually moves in a non-circular orbit about the GC which makes calculation unnecessarily complicated, we define a hypothetical reference point, Local Standard of Rest (LSR), as the reference frame in Galactic coordinates. The LSR is at the same position of the Sun and moves on a circular orbit at  $240 \text{ km s}^{-1}$ . The relative motions of the Sun with respect to this LSR is described by peculiar motion,  $(u_0, v_0, w_0)$ , velocity in radial, tangential and vertical direction respectively (Binney & Merrifield 1998).

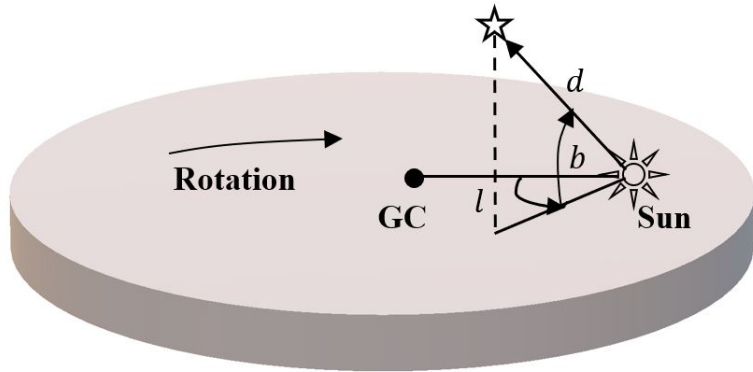


**Figure 2:** A sketch of the Galactic coordinate system.

Assuming the Milky Way has axisymmetric potential and stars are on circular orbits, Oort (1927) derived Oort constants  $A$  and  $B$  via radial velocities and tangential proper motions as a function of Galactic longitude  $l$  by Taylor-expanding the local velocity field to the first order about the LSR. It is shown that the radial velocity

and tangential velocity are proportional to  $\cos 2l$ ,  $\sin 2l$ :

$$v_r = Ad \sin 2l \quad \text{and} \quad v_{\perp} = d(A \cos 2l + B), \quad (1)$$

$$\text{where } A = -\frac{1}{2}\left(\frac{dv_{circ}}{dR} - \frac{v_{circ}}{R}\right)\Big|_{R_{\odot}} \quad \text{and} \quad B = -\frac{1}{2}\left(\frac{dv_{circ}}{dR} + \frac{v_{circ}}{R}\right)\Big|_{R_{\odot}}.$$

In Oort's original measurement, he determined that near the Sun  $A \approx 19$ (km/s/kpc) and  $B \approx 24$  (km/s/kpc) ([Oort 1927](#)). The value,  $A$  describes the local shearing, and  $B$  describes local vorticity. The result of a non-zero  $A$  suggests that stars near the Sun have varying rotation angular velocity, providing the first strong evidence that the Milky Way is rotating differentially.

The Oort constants were generalized to consider the Sun's peculiar motion with respect to nearby stars. It is derived analytically that the double sine (or cosine) trend is distinguishable from the pattern due to the Sun's peculiar motion about nearby stars. Two additional constants were introduced to the function of radial and tangential velocity against  $l$ , namely  $C$ , and  $K$  ([Ogrodnikoff 1932](#)). These four constants,  $A$ ,  $B$ ,  $C$ , and  $K$  describe the transverse shear, vorticity, radial shear, and divergence in the local velocity field from Galactic rotation accordingly. The line of sight velocity ( $v_{los}$ ) is:

$$v_{los} = d(K + C \cos 2l + A \sin 2l) \quad (2)$$

The proper motion in longitude and latitude direction,  $\mu_l$  and  $\mu_b$ , have the following dependence on  $2l$  ([Olling & Dehnen 2003](#)):

$$\mu_l = (A \cos 2l - C \sin 2l + B) \cos b + \varpi(u_0 - v_0 \cos l) \quad (3)$$

$$\mu_b = -(A \sin 2l + C \cos 2l + K) \sin b \cos b + \varpi[(u_0 \cos l + v_0 \sin l) \sin b - w_0 \cos b] \quad (4)$$

In equations above, the single sin and cos terms represent the effect due to the Sun's peculiar motion,  $(u_0, v_0, w_0)$ .

From definition of  $A$  and  $B$  in Eq. 1, the local slope of the rotation frequency ( $\Omega$ ) at the solar radius,  $\frac{d\Omega}{dr}|_{R_{\odot}}$  is  $-(A + B)$ .  $A$  and  $B$  are also related to the local rotation frequency by:  $A - B = \Omega_{\odot} = \frac{v_{circ\odot}}{R_{\odot}}$  at the solar radius. If the Galaxy is not axi-symmetric,  $C$  and  $K$  are nonzero ([Ogrodnikoff 1932](#), [Binney & Merrifield 1998](#)). In the Method section below, I will present the full derivation of Oort constants. The Fourier series approximation approach has also been used to derive Oort constants. The Fourier coefficients of the  $n = 0$  and  $n = 2$  modes correspond to Oort Constants ([Lin et al. 1978](#)).

It must be emphasized that Oort constants can be extended to a set of functions depending on the distances from the Galactic center as we apply Taylor expansion velocity fields about different locations in the MW. Typically, the Oort constants vary at a rate of a few km/s/kpc per kpc ([Olling & Merrifield 1998](#)). For distant stars in the disk, a higher order of the streaming velocity field equation must be taken

into consideration (Siebert et al. 2011). The Oort constants in the first order of the streaming velocity field equation are restrained to the rotation in the solar vicinity because the higher-order contributions will become significant at large distances (Bovy 2017). Due to the contribution from interstellar gas in the MW whose density varies non-monotonically with distance from the Galactic center, between  $0.9R_\odot$  and  $1.2R_\odot$ , the Oort constants  $A(R)$  and  $B(R)$  at varying  $R$  differ significantly from the general angular frequency dependence (Olling & Merrifield 1998). This suggests that when measuring the Oort constants, it is crucial to constrain the range of the Galactic distance.

### 1.3. Measuring Oort constants

In order to measure the Oort constants based on Eqs. 2,3 and 4, we need to have locations and velocities of stars in Galactic coordinates. From our vantage point on Earth, we can get radial velocities from the Doppler shift, and proper motions are measured optically by tracing the stars moving across the plane of the sky. Positions, radial velocities, and proper motions are then converted to Galactic coordinates.

Many investigations have been conducted to attempt to use the proper motions in Galactic coordinates to determine the character of the non-uniformity of rotation and to measure the Oort constants. Fig.3 shows one example of the measurement of Oort constants with proper motions from Bovy 2017. However, not all the results are in agreement Li et al. (2019), which is mainly due to the absence of a complete proper motions catalog. A complete measurement of proper motions can give us stars distant enough that their individual random motions do not dominate general trend of the proper motions. It will also ensure sufficient sky coverage to allow the separation between the double sine curve of Galactic proper motions from the single sine curve due to the solar peculiar motion in Eqs. 2, 3 and 4 (Kerr & Lynden-Bell 1986). Although the observational precisions have been continuously developed, the values of  $A$  and  $B$  are still consistent within uncertainties in different previous investigations. However, for the values of  $C$  and  $K$ , the measurement uncertainties are generally large (Li et al. 2019). Besides needing a complete proper motion catalog, three other factors further complicate an accurate determination of values for the Oort constants.

First, the effect of non-axisymmetric potential associated with the spiral arms or bar structure is not taken into account in Oort's analysis. Observation data suggests the necessity of looking at a non-axisymmetric mode (Metzger et al. 1998). From the radial velocity of Cepheids, a significant zero-point offset (the Oort constant,  $K$ ) in the radial velocities is suggested for a non-axisymmetric model. Metzger et al. (1998) also found a positive antisymmetric ellipticity component at R0. The deviations from the general axisymmetric velocity field, or the deviation from the Oort constants model specified by Eqs. 2, 3 and 4, could be used to study the non-circular motions in great detail and infer the mass associated with the spiral arms (Olling & Merrifield 1998).

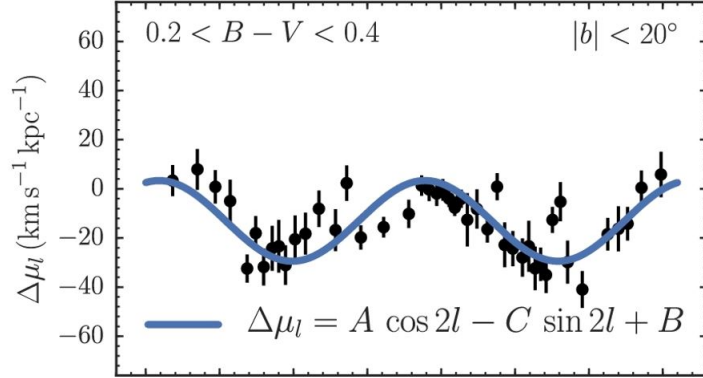


**Figure 3:** One example of the previous measurement of Oort constants from Bovy (2017) with observed proper motion in Galactic longitude: the value on  $y$ -axis is corrected for the solar peculiar motion based on Eq. 3. The averages  $\mu_l(l)$  binned by  $l$  and their errors are plotted.

Second, it is found that moderate strength in the spiral structure causes errors of order 5 km/s/kpc in  $A$  and  $B$  (Minchev & Quillen 2007). The spiral structure can be understood as waves where the spirals have concentrated stars. The streaming motion caused by density waves depending on the local spiral structure is difficult to determine (Lin et al. 1978). Further, the spiral structure raises the level of random motions in the Galactic disk (Sellwood & Carlberg 2014). Determination of other structural parameters to account for the effects from the Milky Way spirals must be made after a basic circular model in Section 1.2.

Third, the nonuniform distribution of stars with measured parallax over longitude in conjunction with the solar peculiar motion contributes to significant  $n = 0$  and  $n = 2$  modes deviated from the first order Oort analysis using Fourier series approximation (Olling & Dehnen 2003). The nonuniform distribution of stars across  $l$  may be due to intrinsic density nonuniformity or observational errors due to the interstellar extinction. This systematic error has a contribution to the longitudinal proper motion  $\mu_l(l)$  indistinguishable from the effect of double  $\sin$  and  $\cos$  dependency. Olling & Dehnen (2003) suggested using the latitudinal proper motions  $\mu_l(l)$  of stars at low latitudes could correct for the errors from mode mixing in Fourier approximation.

#### 1.4. Recent progress based on *Gaia* data

In previous decades, the HIPPARCOS telescope had been used extensively in studying the MW kinematics, including deriving local Oort Constants and the rotation curve from classical cepheid (Feast & Whitelock 1997, Mignard 2000, Olling & Dehnen 2003). The *Gaia* mission (Gaia Collaboration et al. 2016a), since its launch by the European Space Agency in 2013, has collected astrometric parameters with unprecedented accuracy and multitude, aiming to build a three-dimensional map of our Galaxy. By the second release of *Gaia* data, we have the parallax and proper motions of over 1.6 billion stars (Gaia Collaboration et al. 2018). This also includes

stars in higher latitude with significant latitudinal proper motion. Therefore, *Gaia*'s large set of astrometric measurements allows the first truly local precise measurement of the Oort constant and investigation of fine local kinematic features.

Two studies using *Gaia* DR1 and DR2 to calculate the Oort Constants in the solar vicinity yielded results in agreement (Bovy 2017; Li et al. 2019). The current values of the Oort constants based on DR2 are  $A = 15.1 \pm 0.1$ ,  $B = -13.4 \pm 0.1$ ,  $C = -2.7 \pm 0.1$ ,  $K = -1.7 \pm 0.2$ , all in the unit of km/s/kpc (Li et al. 2019). The slope of the rotation curve is determined from  $-(A + B)$  which is negative, thus confirming a slightly declining rotational curve in the solar vicinity. And significant non-zero  $C$  and  $K$  further indicate non-axisymmetric potential (Bovy 2017; Li et al. 2019). This suggests that applying the axis-symmetric assumption of Oort analysis should be carefully examined. Both studies found the local Oort constants varied among different stellar populations based on their positions in the Hertzsprung-Russell Diagram (i.e. stellar age). The result in Li et al. (2019) shows that the red giants deviate from the main-sequence stars in all four constants because they show more elliptical orbits and larger velocity dispersion. This finding is inconsistent with the suggestion in Olling & Dehnen (2003) that red giants are the “true” tracer of the Oort constants because they are old enough to be in equilibrium and distant enough to be unaffected by possible local anomalies. This disagreement suggests establishing an appropriate set of stars is critical to determine Oort constants accurately.

Neither of the previous work using HIPPARCOS and *Gaia* data to fit Oort constants (Bovy 2017, Li et al. 2019) used radial velocity information to determine the local Oort constants because the radial velocity measurement is only available for a fraction of the stars in the *Gaia* data. However, we believe a closer look at the available radial velocity data with comparison to the predicted theoretical model potentially entails significant information.

### 1.5. Motivation of the research

Our work focus on the Main Sequence Stars from *Gaia* DR2. We use their latitudinal and longitudinal proper motions, as well as their radial velocities to determine the local Oort constants in the solar vicinity.

In order to measure Oort constants to higher precision and to understand the influence of sample selection on the final results, this work examines the conventional constraints on data sampling by combining the observational data and numerical simulations. In previous measurements of the Oort constants (Olling & Dehnen 2003; Bovy 2017; Li et al. 2019), the sampling limit on parallax and latitude were explained qualitatively without justification. For example, Olling & Dehnen (2003) suggested to use the longitudinal profile  $\mu_b$  of low latitudes stars to correct for the mode-mixing in deriving the Oort constants mentioned in Section 1.3, while both Bovy (2017) and Li et al. (2019) adopted the  $40^\circ < |b| < 50^\circ$  filtering criteria. Therefore, it is not clear, especially in the case of analyzing  $\mu_b$ , which subsets of stars in observation data

should be used to derive the Oort constants and how using different subsets affects the final results.

We also use a simple 3D toy model of simulated test particle under the near circular orbital motion assumption to obtain a theoretical prediction of longitudinal and latitudinal proper motion,  $\mu_l$  and  $\mu_b$ , and radial velocity  $v_{los}$  as functions of Galactic longitude  $l$ . The simulation samples 500,000 test particles moving under the axisymmetric MW potential specified by [Bovy \(2015\)](#). The goal of this model simulation and comparing it to observational data is twofold. First, it allows us to find the range of parallax and Galactic latitude that give the best stellar subset(s) for Oort constants measurement. Second, it helps us to characterize the deviations in *Gaia*'s observational result from the expected model. The larger significance of this work is to provide a sample selection guidance for future Oort constants analysis.

In addition, to derive the Oort constants and their uncertainties, this work applied the Monte Carlo Markov Chain(MCMC) method to fit both observational results from *Gaia* and the simulation results of the toy model to Eqs. 2, 3 and 4. Details of the sample selection, MCMC fitting, and simulation are be included in the following sections. In the result section, we explore the connection between our simulation and DR2 observational data. We hope the result of this work will give some guidance and insights into deriving the Oort constants from more complete catalogues in the near future, for example, the recent early third release of *Gaia* in December 2020 which has added 200 million new samples to our database ([Gaia Collaboration et al. 2020](#)).

## 2. METHODS

### 2.1. *Derivation of The Oort constants*

The Oort constants describe stellar streaming motions about the Sun in the Galactic coordinate, a left-handed coordinate where the direction from the Sun to the Milky Way (MW) galactic center is longitude  $l = 0$  and positive  $x$  (Fig 2). Consider a flat 2D Galactic disk under axisymmetric potential and the cold limit in which all stars move on near circular orbits e.g. as defined in [Olling & Dehnen \(2003\)](#). The position of a star on the disk is  $(x, y)$ , where  $(0, 0)$  is at the Sun in the Galactic coordinate. The velocity field  $\langle v \rangle$  gives the average velocity at each point on the disk. Assuming the Sun is on a pure circular orbit, in the solar vicinity, the velocity at  $(x, y)$  may be expanded in a Taylor series about the Sun:

$$\langle v \rangle|_{(x,y)} = \langle v \rangle|_{(0,0)} + \begin{pmatrix} v_{xx}, v_{xy} \\ v_{yx}, v_{yy} \end{pmatrix} \Bigg|_{(0,0)} \begin{pmatrix} x \\ y \end{pmatrix} \quad (5)$$

$$= \langle v \rangle|_{(0,0)} + \begin{pmatrix} K + C, A - B \\ A + B, K - C \end{pmatrix} \Bigg|_{(0,0)} \begin{pmatrix} x \\ y \end{pmatrix}, \quad (6)$$

where A, B, C and K are the Oort constants. The relative velocity of the star as observed from the Sun is given by

$$\delta\langle v \rangle|_{(x,y)} = \langle v \rangle|_{(x,y)} - \langle v \rangle|_{(0,0)}. \quad (7)$$

The line of sight velocity is the component of  $\delta\langle v \rangle$  parallel to the galactic distance  $d$ :

$$v_{los} = \hat{d} \cdot \delta\langle v \rangle = \frac{(x, y)}{d} \cdot \begin{pmatrix} K + C & A - B \\ A + B & K - C \end{pmatrix} \Big|_{(0,0)} \begin{pmatrix} x \\ y \end{pmatrix}. \quad (8)$$

After taking the dot product and applying trigonometric relations, we have

$$v_{los} = d[K + A \sin(2l) + C \cos(2l)] \quad (9)$$

Similarly, the longitudinal proper motion, perpendicular component of the relative velocity over  $d$ , is:

$$\mu_{\perp} = \frac{1}{d}(\hat{d} \times \delta\langle v \rangle) = B + A \cos(2l) - C \sin(2l) \quad (10)$$

Recall the introduction of the Galactic coordinates and the local standard of rest (LSR) above Fig. 2 in Section 1.2. Thus, Eqs. 9 and 10 in fact describe the relative motions relative to the LSR. After correcting the solar peculiar motion, the two equations turn into:

$$v_{los} = d[K + A \sin(2l) + C \cos(2l)] - u_0 \cos(l) - v_0 \sin(l) \quad (11)$$

$$\mu_l = B + A \cos(2l) - C \sin(2l) + \frac{1}{d}[u_0 \sin(l) - v_0 \cos(l)], \quad (12)$$

where the  $\cos b$  term in Eq. 12 accounts for the projection of distance onto the Galactic plane in a 3D MW disk. If the vertical velocity  $v_z$  of the star is non-zero, the latitudinal relative velocity at  $(l, b, d)$  is given by  $v_z(\cos b) - v_{los} \sin(b)$  (Olling & Dehnen 2003), and the latitudinal proper motion is:

$$\mu_b = -(A \sin 2l + C \cos 2l + K) \sin b \cos b + \varpi[(u_0 \cos l + v_0 \sin l) \sin b - w_0 \cos b], \quad (13)$$

where  $\varpi$  is parallax and its inverse gives the distance from the Sun.

## 2.2. The Gaia Sample selection and stellar parameter estimation

The *Gaia* (Global Astrometric Interferometer for Astrophysics) mission of the European Space Agency (ESA) surveys about one billion stars in the MW photometrically and spectroscopically to make the most accurate three-dimensional map of the Galaxy. In 2018, ESA released the second intermediate data DR2. This version of release catalogs the positions and proper motions, and other photometric data of 1.3 billion million data in DR2 after deleting. *Gaia* samples kinematic tracers to a magnitude limit of at least  $G = 20$  mag in the MW disks, bulge, and halo. The instrument

package of *Gaia* spacecraft comprises two identical optical telescopes/imaging systems, a radial velocity spectrometer, and blue and red photometers. The unfiltered, white-light photometric  $G$  band of the optical telescope covers 330–1050 nm ([Gaia Collaboration et al. 2016](#)). The parallax uncertainties are 0.5 mas at  $G = 20$ . The uncertainties in proper motion are 0.5 mas yr $^{-1}$  at  $G = 20$  ([Gaia Collaboration et al. 2018](#)).

The radial-velocity spectrometer obtains radial velocities by measuring the Doppler-shift in the lines of stellar spectra. DR2 has the radial velocity of more than 7.2 million stars with a mean  $G = 4 - 13$  mag and an effective temperature in the range 3550 to 6900 K. The overall precision of the radial velocities range from 200–300 m s $^{-1}$  to 1.2–3.5 km s $^{-1}$  ([Gaia Collaboration et al. 2016](#)). Astrophysical parameters such as effective temperature, surface gravity, metallicity of the stars, and extinction are derived from the BP and RP data measured by the blue and red photometers over the wavelength ranges 330–680 nm and 630–1050 nm ([Gaia Collaboration et al. 2016](#)). In December 2020, ESA made the third early release (EDR3) which added more than 100 million entries to the original DR2 catalogue. We used the TAP service from TOPCAT (Tool for Operations on Catalogues And Tables) to access, process, and select the DR2 data ([Taylor 2005](#)). (Appendix 6.1 discusses the reason why this work does not analyze EDR3.)

In Eq. 6, since the first-order Taylor approximation is only appropriate for the solar vicinity, the stellar samples are limited to the region within 500 pc (2mas) from the Sun. And restricting parallax/error  $\geq 10$  will avoid additional bias from inverting the parallax to estimate distance ([Luri et al. 2018](#)). The uncertainties in the BP and RP fluxes are restrained to less than 10% in making the Hertzsprung–Russell (H-R) diagram and selecting the main sequence samples. Potential duplicate sources are also removed. In sum, the query criteria in TOPCAT are the following:

```
parallax > 2, parallax/parallax_error > 10,
phot_BP_mean_flux_over_error > 10, phot_RP_mean_flux_over_error > 10,
duplicated_source = 0
```

The main sequence stars are selected by drawing on the H-R diagram in TOPCAT after parallax correction, color excess and extinction are considered in Fig. 4. Because the local Oort constants varied among different stellar populations based on their color, thus their collective kinematic properties, we group the main sequence stars into six color groups on the H-R diagram based on color according to the criteria of [Li et al. \(2019\)](#). The rotational kinematics properties and the corresponding Oort constants for color group are analyzed individually. Table1 shows the number of stars in each stellar group, as well as the corresponding numbers in DR2.

The proper motions and radial velocity entries in *Gaia* are measured in the equatorial coordinates system (ICRS), i.e. right ascension ( $\alpha$ ) and declination ( $\delta$ ) proper motions,  $\mu_\alpha$  and  $\mu_\delta$ . I used the SkyCoord class in *astropy* ([Astropy Collaboration](#)

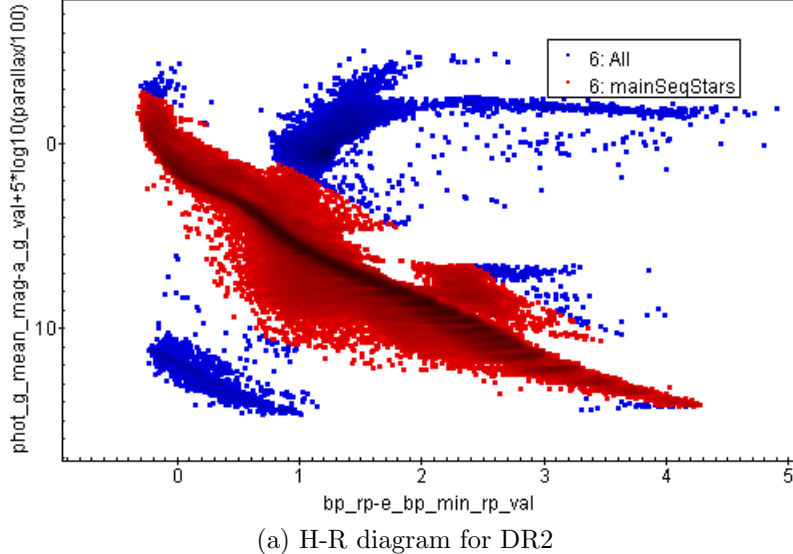


**Figure 4:** the H-R diagram and Main sequence star samples in DR2 after parallax, extinction and color excess correction.

$BP - RP - E(BP - RP)$	$< 0.8$	$0.8 - < 1.2$	$1.2 - 1.6$	$1.6 - < 2.0$	$2.0 - 2.4$	$\geq 2.4$
DR2	978428	1591020	1284402	1086626	865742	351820

**Table 1:** Number of main sequence stars fall into each color group in DR2.

et al. 2018) to transform proper motions and available radial velocity from ICRS to the Galactic coordinate. The units of proper motion are also converted from mas/yr to km/s/ kpc by multiplying a factor of 4.74047.

### 2.3. Estimating the Oort constants from Gaia DR2 data

For each stellar group in Table1, we use the following process to derive the corresponding Oort constants from  $\mu_l$ ,  $\mu_b$  and  $v_{los}$ .

We first convert the proper motions and radial velocities from ICRS to the Galactic coordinates. As we will see in the result section,  $\mu_l$  is the more reliable tracer to derive the Oort constants, and only the first two bluest color groups have  $v_{los}$  measurement available for most of the entries. Rearranging Eq. 12, we define  $\Delta\mu_l$  as :

$$\Delta\mu_l = \frac{1}{\cos b}(\mu_l - \varpi(u_0 \sin(l) - v_0 \cos(l))) = A \cos 2l + B \sin 2l + C. \quad (14)$$

We use all the individual  $\mu_l$  to find the solar peculiar motion  $(u_0, v_0, w_0)$  such that the binned medians of  $\Delta\mu_l$  with bin width of  $l = 5^\circ$  after removing any outlying values fit to  $A \cos(2l) + B \sin(2l) + C$  by maximum-likelihood estimation method. Eq. 14 constrains the value of  $u_0$  and  $v_0$  in the solar peculiar motion, but not for  $w_0$ . Therefore, we use  $w_0 = 7.25$  km/s from Schönrich et al. (2010) together with the  $u_0$  and  $v_0$  estimated from  $\Delta\mu_l$  above to find  $\Delta\mu_b$  and  $\Delta v_{los}$  by rearranging Eqs. 13 and

11:

$$\Delta\mu_b = -\frac{1}{\sin b \cos b}(\mu_b - \varpi[(u_0 + v_0) \sin b - w_0 \cos b]) = A \sin 2l + C \cos sl + K, \quad (15)$$

$$\Delta v_{los} = \varpi(v_{los} + u_0 \cos l + v_0 \sin l) = A \sin 2l + C \cos sl + K. \quad (16)$$

Then we estimate the Oort constants from  $\Delta\mu_l$  and  $\Delta v_{los}$  respectively.

#### 2.4. Estimating the parameters and their corresponding uncertainties:

##### Monte-Carlo-Markov-Chain

In Eqs. 14, 15 and 16, the parameters of each model are the three Oort constants. And when we consider  $\Delta\mu_l$  and  $\Delta\mu_b$  together in estimating the Oort constants, the model parameters are the four Oort constants. For such a high-dimensional parameter space, we use the Monte Carlo Markov Chain (MCMC) method to determine the value and uncertainty of each parameter. The MCMC method combines our prior knowledge about the model and evidence from the data to obtain a posterior distribution of the model parameter  $\theta$ , in this case,  $\theta(A, B, C)$ ,  $(A, C, K)$  or  $(A, B, C, K)$ .

MCMC method randomly samples a parameter model from the parameter distribution based on our prior knowledge, and evaluate how our data is likely for this particular model. This likelihood is called the posterior likelihood function. MCMC then uses the process of Markov chain to "walk" around the high-dimension parameter space until it finds the set of parameter values that maximizes the posterior likelihood function. The posterior combines a prior distribution on the model parameter  $\theta$  and a logarithmic likelihood function that quantifies how well our data support the parameter model. For example, if we derive the Oort constants by considering  $\Delta\mu_l$  and  $\Delta v_{los}$  together, the corresponding logarithmic likelihood function weighted by errors is defined as:

$$\ln \mathcal{L} = - \sum_i \left( \frac{(\langle \Delta\mu_l \rangle_i - y_{1i})^2}{\sigma_{\langle \Delta\mu_l \rangle}^2 + error_{\langle \Delta\mu_l \rangle i}^2} + \ln \frac{2\pi}{\sigma_{\langle \Delta\mu_l \rangle}^2 + error_{\langle \Delta\mu_l \rangle i}^2} \right. \\ \left. - \frac{\langle \Delta v_{los} \rangle_i - y_{2i}^2}{\sigma_{\langle \Delta v_{los} \rangle}^2 + error_{\langle \Delta v_{los} \rangle i}^2} + \ln \frac{2\pi}{\sigma_{\langle \Delta v_{los} \rangle}^2 + error_{\langle \Delta v_{los} \rangle i}^2} \right) \quad (17)$$

where  $\sigma_{\langle \Delta\mu_l \rangle}$  and  $\sigma_{med(\mu_b)}$  are the Gaussian scatter for the distribution of binned medians,  $error_{\langle \Delta\mu_l \rangle i}$  and  $error_{\langle \Delta\mu_l \rangle i}$  are the standard deviations within each bin, and  $y_1$  and  $y_2$  are given by Eqs. 14 and 16 (Li et al. 2019).

The prior distribution of  $\theta$  is defined as following:

$$P(\theta) = \begin{cases} 0 & \text{if } 10 < A < 20, -15 < B < -5, -5 < C < 5, \text{ and } -5 < K < 5 \\ -\infty & \text{if } A, B, C \text{ and } K \text{ are not within the range above} \end{cases} \quad (18)$$

And the overall logarithmic posterior probability is:

$$LnP(\theta|y) = \begin{cases} lnL & \text{if } P(\theta) = 0 \\ 0 & \text{if } P(\theta) = -\infty \end{cases} \quad (19)$$

MCMC uses multiple Markov chains that start at slightly different initial parameter values. All Markov chains eventually converge in the high probability region of the parameter space. We use the standard deviation of the final value of each parameter in  $\theta$  after all Markov chain converges as the uncertainties of the derived Oort constants. We employ the *emcee* (Foreman-Mackey et al. 2013) python package to sample and update the Markov chains in MCMC.

### 2.5. Test particle simulation

To know what behaviors are expected from the theoretical Oort constants model, and thus understand how the actual MW deviates from the theoretical model, we constructed a toy model simulation, treating stars as test particles in a fixed MW potential and assuming all the model constraints of the Oort constants and the Sun stays on a circular orbit. I sampled 500,000 of test particles from *AGAMA*'s quasi-isothermal distribution function to represent a thin 3D Milky Way galactic disk (Vasiliev 2019). The distance from the Sun to the Galactic center and the circular velocity at the solar radius are set to  $R_0 = 8.34$  kpc and  $v_0 = 240$  km/s respectively. The horizontal scale of the disc is 0.4 kpc, and the radial velocity dispersion is chosen as 10km/s. This distribution function provides planar and vertical profiles of the thin disc with analytic function dependent on the action integrals in an integrable, axisymmetric Hamiltonian (Binney 2010). The Galactic potential in the Hamiltonian is specified by MWPotential2014 (Bovy 2015).

MWPotential2014 serves as a simple and accurate model for the MW potential from fitting to a large variety of dynamical data. This potential model consists of a bulge potential with a power law exponent of 1.8 and a cut-off radius of 1.9kpc (PowerSphericalPotentialwCutoff), a disk potential specified by MiyamotoNagaiPotential, and a dark-matter halo described by an NFWPotential (Bovy 2015). Fig 5 shows the spatial distribution of test particles sampled from the quasi-isothermal distribution function.

Besides, because we set the peculiar motion of the Sun to 0, the coordinate and velocity of LSR and the Sun are equivalent. All particles undergo 10Gyr of orbit integration under the potential specified by MWPotential2014 to reach equilibrium. The positions and velocities after 10Gyr are then used to calculate  $\mu_l$  and  $\mu_b$ , as well as  $v_{los}$ . Similar to the procedure of analyzing *Gaia* data, I binned the simulation data and used the binned medians to estimate the three equations in Eq 11, 12 and 13 by MCMC, except  $u_0$ ,  $v_0$ , and  $w_0$  are set to 0.

## 3. RESULTS

### 3.1. Simulation: The effect of sampling criteria on $\mu_l$ , $v_{los}$ , $\mu_b$

From the simulation with 500,000 stars (test particles) described in above (Section 2.5), we examined the effect of different sampling criteria on the resulting proper motions ( $\mu_l$  and  $\mu_b$ ) and the line-of-sight velocity ( $v_{los}$ ) dependency on  $l$ . Fig 5a displays the distribution of all the particles in 16 kpc from the GC and  $\pm 4$  kpc in

the vertical direction. This disc looks thicker despite the scale height in the quasi-isothermal distribution function (Section 2.5) was set to 0.4 kpc because the tail of exponential distribution is evident when sample size is large. In Fig 5b, we show those stars within  $d = 3$  kpc from the Sun. We replicate the Sun's position at four symmetric positions  $(8.34\text{kpc}, 0, 0)$ ,  $(0, 8.34\text{kpc}, 0)$ ,  $(-8.34\text{kpc}, 0, 0)$  and  $(0, -8.34\text{kpc}, 0)$  in the Cartesian form of the Galactocentric coordinate. This strategy increases the number of stars nearby the Sun(s) to give us robust results to derive the Oort constants.

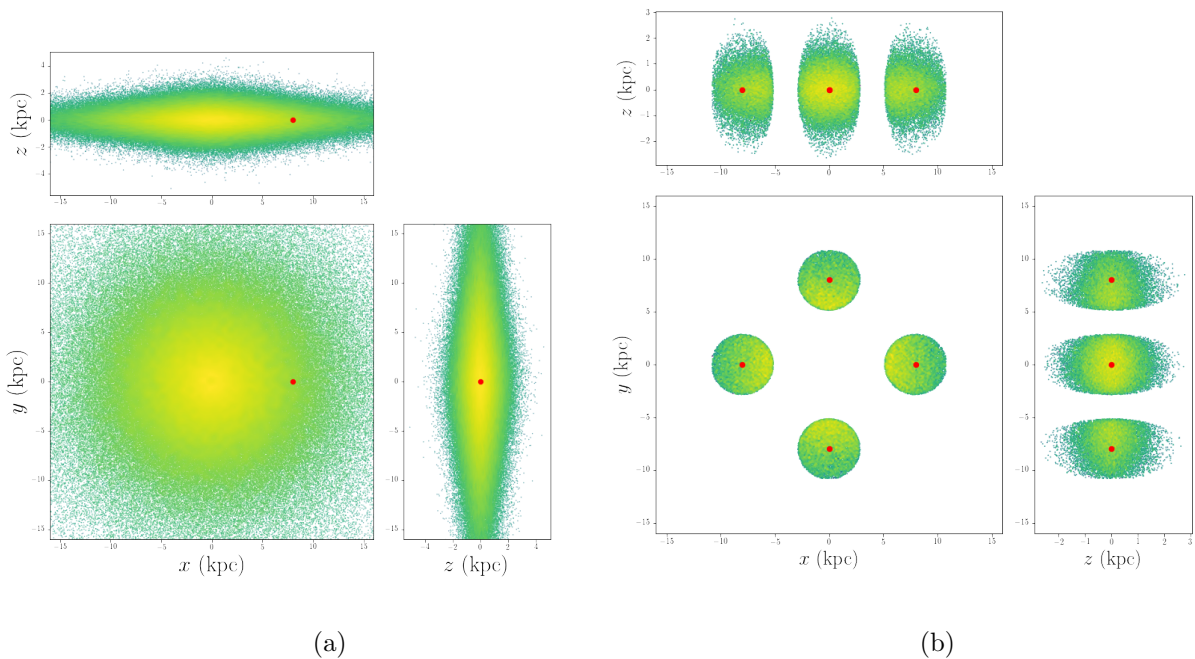
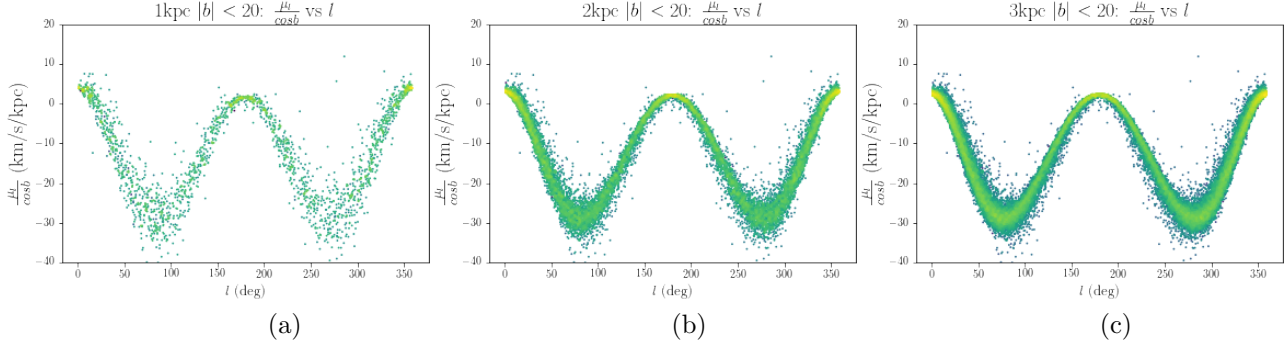


**Figure 5:** (a) The distribution of the 500,000 test particles (stars) sampled from quasi-isothermal distribution function for the Milky Way. (b) The distribution of simulated stars within  $d = 3$  kpc from the Sun, where we replicate the Sun at four different symmetric positions to increase the sizes of effective samples near the Sun. Brighter color corresponds to a higher density

### 3.1.1. $\mu_l$ and $v_{los}$

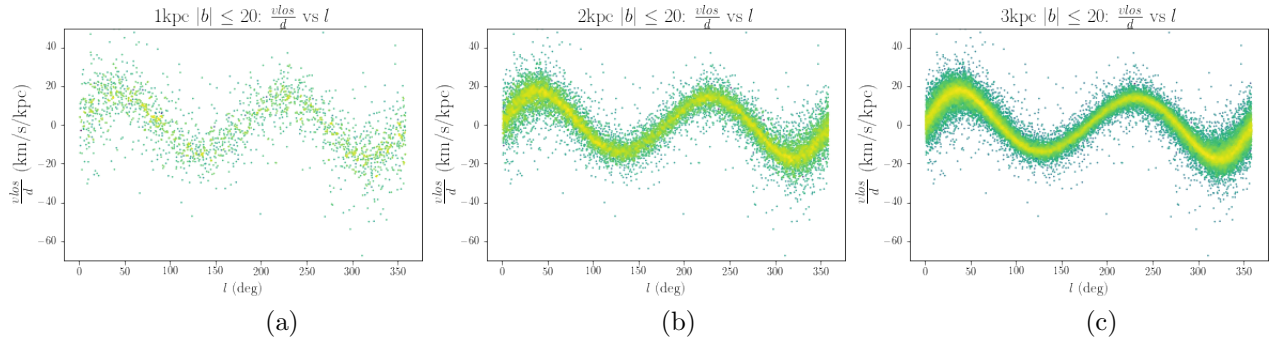
In Fig 6, we present the result of  $\mu_l$  vs  $l$  under three sample filtering criteria on the galactic distance  $d$  for stars that approximately lie on the mid-plane ( $|b| < 20^\circ$ ). Proper motions after correcting the contribution in latitudinal direction ( $\cos b$ ) are mostly negative across  $l = 0^\circ$  to  $360^\circ$ , indicating that stars move in the decreasing  $l$  direction. Fig 6 also shows that  $\mu_l$  has slightly positive value at  $l = 0^\circ, 180^\circ$ , and  $360^\circ$ .  $\mu_l$  is most negative and has relatively larger variation among stars with the same  $l$  value at  $l = 90^\circ$  and  $270^\circ$  compared to the stars at  $l = 0^\circ, 180^\circ$ , or  $360^\circ$ . In

Fig. 6a, the standard deviation of  $\mu_l / \cos b$  at  $l = 0^\circ$  is 0.54 km/s/kpc, while 4.00 km/s/kpc at  $l = 90^\circ$ .



**Figure 6:** The distribution of  $\mu_l / \cos b$  over  $l$  for stars with  $|b| \leq 20$  and ,(a)  $d \leq 1$  kpc,(b)  $d \leq 2$  kpc, and (c)  $d \leq 4$  kpc

In Fig 7, we see for stars with  $d < 2$  kpc and  $|b| < 20$ ,  $v_{los}$  after divided by  $d$  traces a single double sinusoidal function as expected from Eq. 11.  $v_{los}$  is 0 at  $l = 0^\circ, 90^\circ, 180^\circ, 270^\circ$ . Positive  $v_{los}$  between  $l = 0^\circ$  to  $90^\circ$  and  $l = 180^\circ$  and  $270^\circ$  suggests that stars move away from the Sun in the line of sight direction in these two  $l$  intervals. And stars approach the Sun in the line of sight direction between  $l = 90^\circ$  and  $180^\circ, 270^\circ$  and  $360^\circ$ . We show the comparison of  $v_{los}/d$  vs  $l$  if we keep  $|b| < 20^\circ$  but constrain to stars to within 1kpc in Fig 7a and within 3kpc in 7c.



**Figure 7:** The distribution of  $v_{los}/d$  over  $l$  for stars with  $|b| \leq 20$  and (a)  $d \leq 1$  kpc,(a)  $d \leq 2$  kpc, and (c)  $d \leq 4$  kpc

In Fig 8 , we use two simple schematic diagrams of stars to illustrate the expected variation of  $\mu_l$  and  $v_{los}$  as a function of the Galactic longitude. We assume these stars are all in circular orbits with radius  $R_{star}$  around the GC. At  $l = 0^\circ$  and  $180^\circ$ ,  $v_\phi$  is in the line of LSR, and  $v_\phi$  is perpendicular to the line of sight. As a result,  $v_{los} = 0$  and  $v_l = v_\phi - v_{\phi\odot}$ . According to the rotation velocity curve in (Fig 1), the radial profile of  $v_\phi$  is flat while slightly declining at  $R = R_\odot$ . As a result, the star moves in the

direction of increasing  $l$ , giving  $\mu_l$  a small positive value at  $l = 0^\circ$  in the inner side of the MW disk. At  $l=180$ , because  $v_\phi$  is smaller than  $v_{\phi\odot}$ , the star lags behind the Sun, moving in the direction of increasing  $l$ , thus  $\mu_l$  is expected to be positive (Fig 8b).

At  $l = 90^\circ$  and  $270^\circ$ , stars are approximately in the same circular orbits as the Sun. They are essentially moving at the same speed as the Sun along the line of sight, thus  $v_{los} = 0^\circ$ . However, to examine their proper motion, we need to zoom in closer to show that  $v_{phi}$  varies slightly in their direction. And Fig 8b shows the perpendicular component  $v_l$  points in the decreasing  $l$  direction at both  $l = 90^\circ$  and  $270^\circ$ .

At  $l = 45^\circ$ ,  $225^\circ$ ,  $l = 135^\circ$  and  $315^\circ$ , the orange vectors in Fig 8a and 8b indicate the relative velocity in the line-of-sight and tangential  $l$  direction after comparing to the velocity of the Sun in each direction respectively. We show that at  $l = 45^\circ$ ,  $v_{los} > 0$  and  $v_l < 0$ ;  $l = 45^\circ$ ,  $v_{los} < 0$  and  $v_l < 0$ ;  $l = 135^\circ$ ,  $v_{los} > 0$  and  $v_l < 0$ ;  $l = 225^\circ$ ,  $v_{los} > 0$  and  $v_l < 0$ ;  $l = 315^\circ$ ,  $v_{los} > 0$  and  $v_l < 0$ .

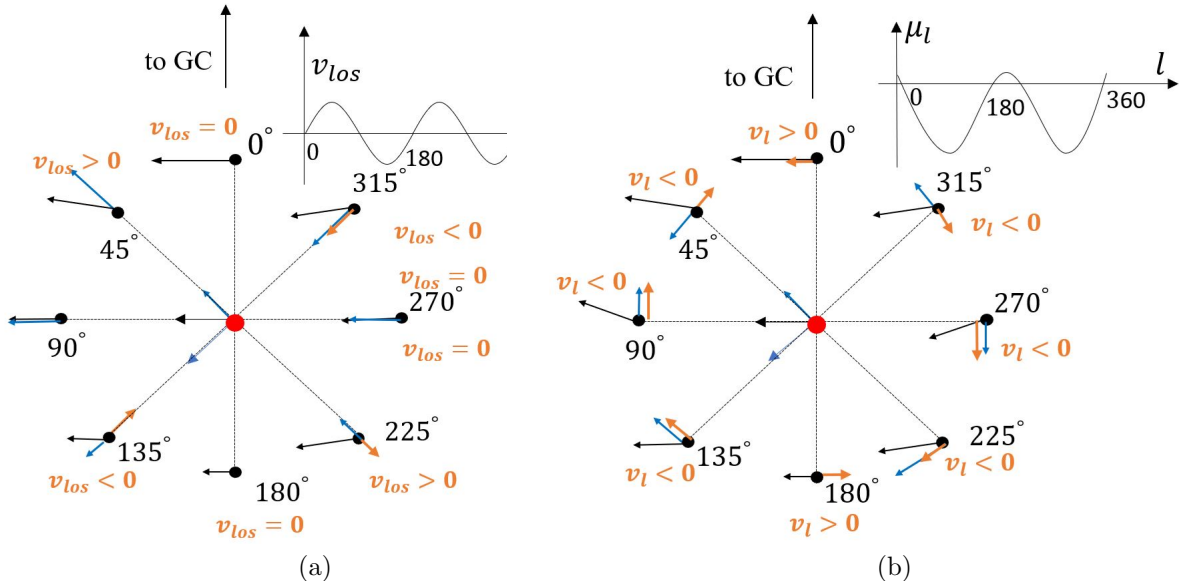


**Figure 8:** The variation in the radial velocity and transverse velocity among different Galactic longitude due to differential rotation of the Milky Way. The black arrows represent the velocity vector of  $v_\phi$ . The blue vectors represent the components in the line of sight direction (Fig 8a) and the longitudinal direction (Fig 8b). The orange arrows are the relative velocity vectors in the two directions after taking the circular motion of the Sun into account.

### 3.1.2. The effect of the distance selection on the longitudinal profiles of $\mu_l$ and $v_{los}$

In Figs. 6 and 7, the number of samples selected drops from 51196 to 16741 and to 2310 as the galactic distance cut-off decreases from 3kpc, to 2kpc, and to 1kpc.

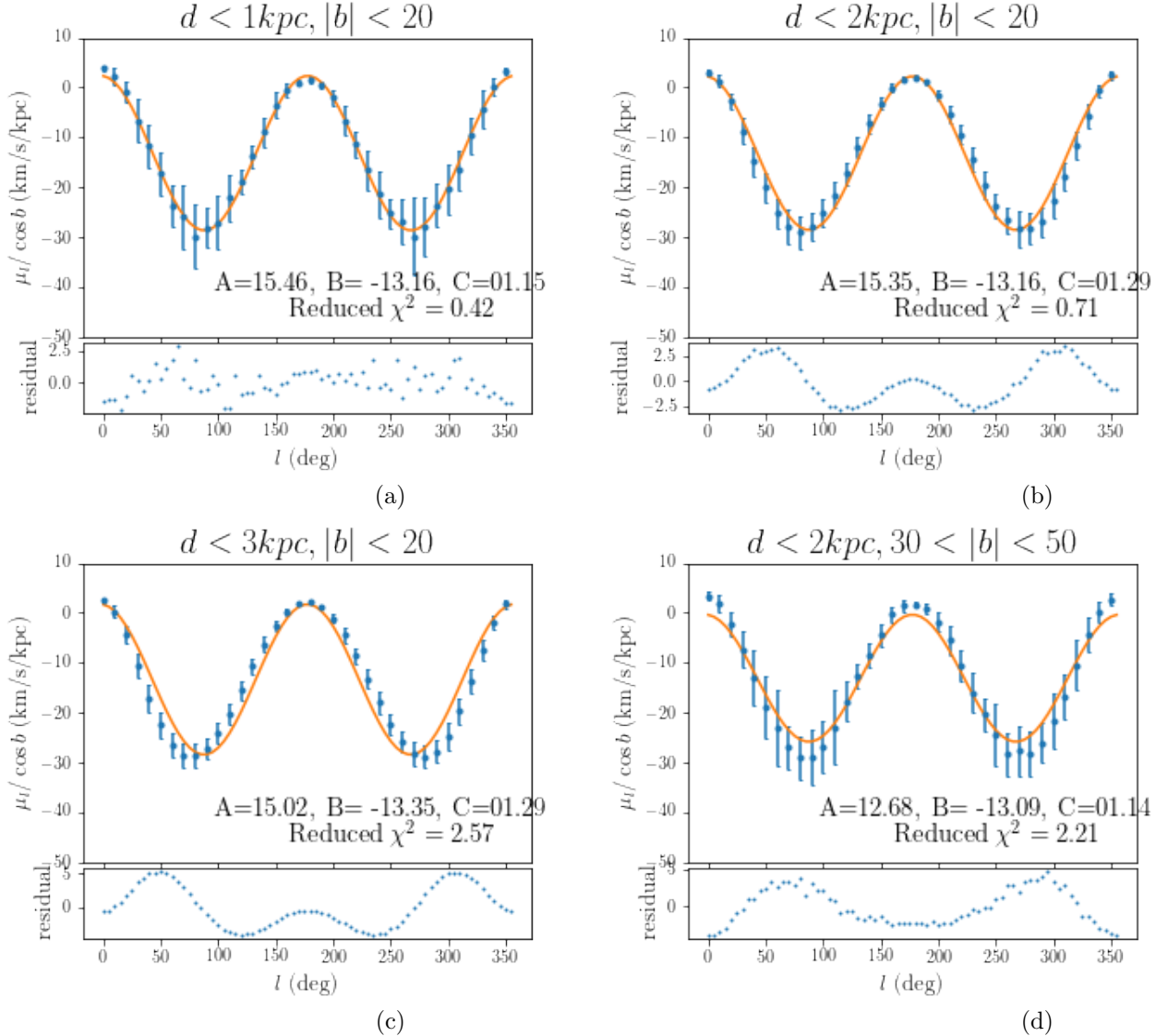


**Figure 9:** The function of binned median  $\mu_l / \cos b$  over  $l$  for stars with  $|b| \leq 20^\circ$  and (a)  $d \leq 1\text{kpc}$ , (b)  $d \leq 2\text{kpc}$ , and (c)  $d \leq 4\text{kpc}$ . The orange continuous curves come from fitting the binned median data to Eq. 12 with maximum likelihood approximation. Only 36 out of 72 binned medians are plotted. The bottom panel for each subplot includes the residual profile.

While the dispersion of  $\mu_l / \cos b$  and  $v_{los}/d$  are unaffected by the distance cut-off chosen in Fig. 6, the binned median values reveal some differences. In Fig 9, all the scatter data of Fig 6 are grouped into bins with a width of  $l = 5^\circ$ , and the median of  $\mu_l$  in each bin is plotted against  $l$ . The error bars are the standard deviations of the corresponding bins. For simulated stars within 3kpc, although the general trend is similar to the  $\cos(2l)$  curves, there are non-negligible deviations from the double cosine function (Fig. 9c). This result suggests that 3kpc is too large for the first-order

Taylor expansion around the Sun in Eq. 6. The stars within 2kpc yield a reduced  $\chi^2$  closest to 1. The proper motions of stars within 1kpc from the sun trace the double sinusoidal function best compared to 2kpc and 3kpc, and the residuals are also smallest for this group. However, this galactic distance cut-off only yielded 2310 out of 500,000 that meet this filtering criteria. The standard deviation within each bin is larger possibly because a smaller sample size is more subjective to the difference between individual values and the medians.

Similarly, the binned  $v_{los}$  median of stars within  $d < 1\text{kpc}$  and  $|b| < 20^\circ$  give  $v_{los}/d$  vs  $l$  closest to the function in Eq. 11 compared to the stars within 3kpc and 2kpc. The reduced  $\chi^2$  values calculated for all the fittings in Figs. 9 and 10 do not give informative measurements on the goodness of the fit. Reduced  $\chi^2$  being much larger than 1 suggests errors are underestimated, and overestimated for Reduced  $\chi^2$  being much smaller than 1. However for our simulated data, the errors come from standard deviation within each bin. Instead, we look at the range and distribution in the residual vs  $l$  profile to decide if the fit is satisfactory. For both  $\mu_l / \cos b$  and  $v_{los}/d$ , the residual profiles for  $d < 1\text{kpc}$  have the smallest ranges. Moreover, for the fittings of  $d < 2\text{kpc}$  or  $d < 4\text{kpc}$  samples, the residual distribution is not uniform above or below 0 but exhibits a clear dependency on  $l$ , while when  $d < 1\text{kpc}$ , residuals are distributed randomly above and below 0. The dependency of residuals on  $l$  seems worthy of further investigation in future work. as it may hint to additional velocity structures.

### 3.1.3. The effect of Galactic latitude range on the longitudinal profiles of $\mu_l$ and $v_{los}$

In second row of Fig 9, we compare the binned  $\mu_l$  median vs  $l$  of stars at  $d < 2\text{kpc}$  from the Sun but at different latitude ranges,  $|b| < 20^\circ$ ,  $30^\circ < |b| < 50^\circ$  and  $60^\circ < |b| < 80^\circ$ . The scatter in the  $\mu_l$  around the central double sinusoidal line increases for higher latitude regions as suggested by the error bars on the binned median data. When  $|b| \leq 20^\circ$ , stars are considered close to the MW mid-plane, thus are most suitable to fit the model in Eq. 12. For  $30^\circ \leq |b| \leq 50^\circ$ , the scattered data deviate from the double cosine function considerably. And for  $60^\circ \leq |b| \leq 80^\circ$ , not only the spread in the scattered data is the largest, the binned medians deviate from the fitted double cosine function more significantly according to the residual vs  $l$  panel in Fig 9.

Likewise, in Fig 10, the spread in the  $v_{los}/d$  of the stars within 2kpc from the Sun but at a higher latitude  $b$  is larger. Comparing the residual profiles in the lower panels, we see the range of residuals is the smallest for the group closest to the MW mid-plane. This suggests that the deviation of binned  $v_{los}/d$  median from the predicted double sine function is smallest for stars at  $|b| < 20^\circ$  and largest at  $60^\circ < |b| < 80^\circ$ . With a larger latitude limit, we move away from the Milky Way disk, and the orbits get less circular. MW potential gradient in the z-direction is large enough to add significant vertical perturbations at high latitude region, tilting the circular orbits. Therefore,

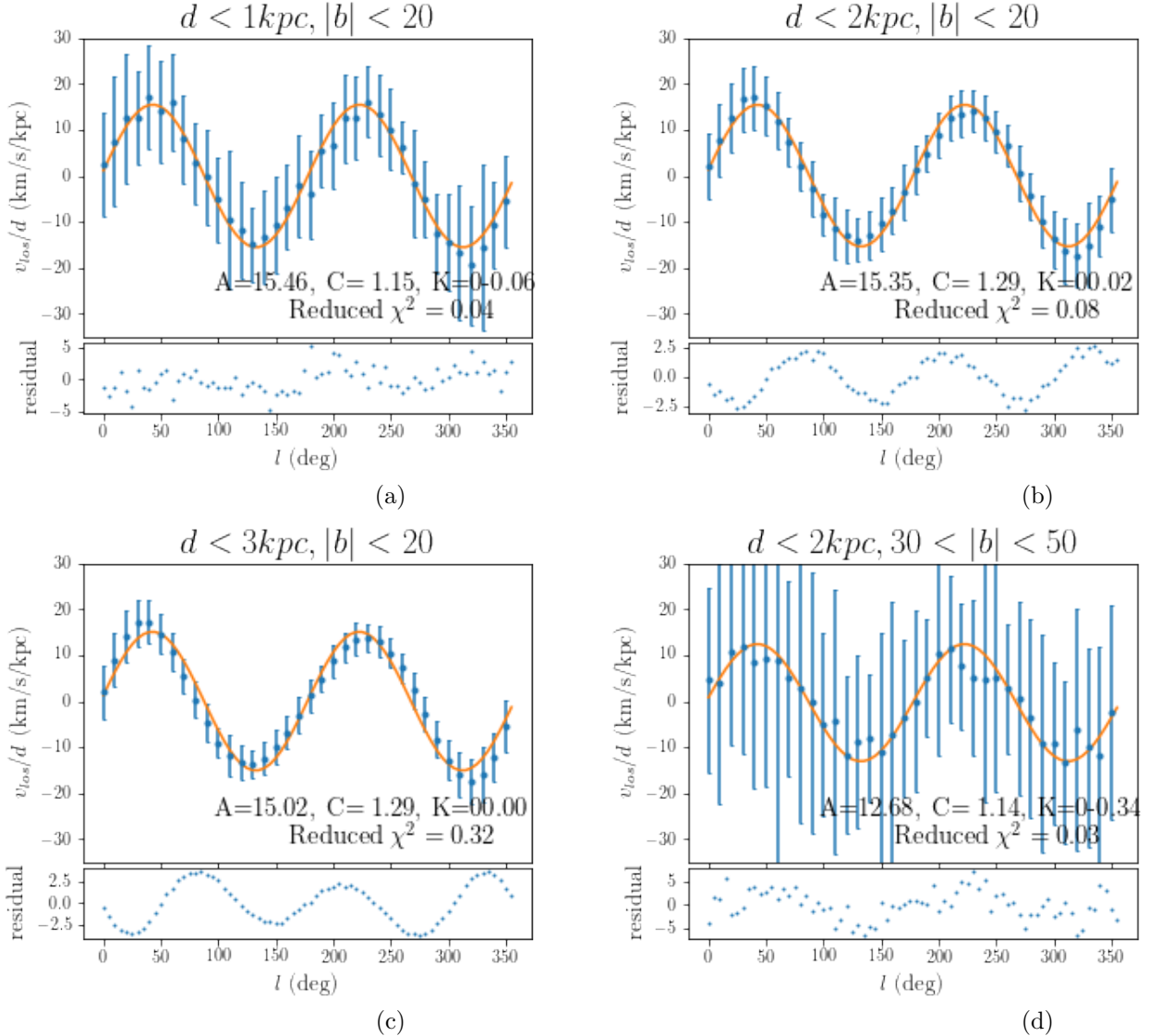


**Figure 10:** The longitudinal profiles of the binned median  $v_{\text{los}}/d$  over  $l$  for stars with  $|b| \leq 20^\circ$  and (a)  $d \leq 1\text{kpc}$ , (b)  $d \leq 2\text{kpc}$ , and (c)  $d \leq 4\text{kpc}$ . The orange continuous curves come from fitting the binned median data to Eq. 11 with maximum likelihood approximation. Only 36 out of 72 binned medians are plotted.

we expect that the deviation is significant for stars at  $60^\circ < |b| < 80^\circ$  in the solar vicinity.

### 3.1.4. Longitudinal profiles of $\mu_b$

For proper motion in the latitude direction,  $\mu_b$ , we expect to see more nonzero value at the region aways from the Galactic plane with relatively larger latitude because of the product  $\sin b \cos b$  in Eq. 13. In Fig 11, contrast to  $\mu_l$  and  $v_{\text{los}}$  discussed above, the value of  $\mu_b/\cos b \sin b$  of stars with  $d < 2\text{kpc}$  and  $30 < |b| < 50$  are much more dispersed. In Fig 13, taking binned medians gives the double sinusoidal curve

expected from Eq. 13. The binned standard deviations for these binned  $\mu_b$  medians range from 50-100 km/s/kpc, much larger than the variation of the binned medians across  $l$ , ( $\pm 25$  km/s/kpc). Thus, error bars are not plotted in Fig 13 to better show the variation of binned  $\mu_b/\cos b \sin b$  medians on  $l$ . At  $l = 0^\circ, 90^\circ, 180^\circ, 270^\circ$ ,  $\mu_b = 0$ . Stars are descending from the perspective of LSR from  $l = 0$  to  $90^\circ$  and from  $180$  to  $270^\circ$  while ascending from  $l = 90^\circ$  to  $180^\circ$  and from  $270^\circ$  to  $360^\circ$ .

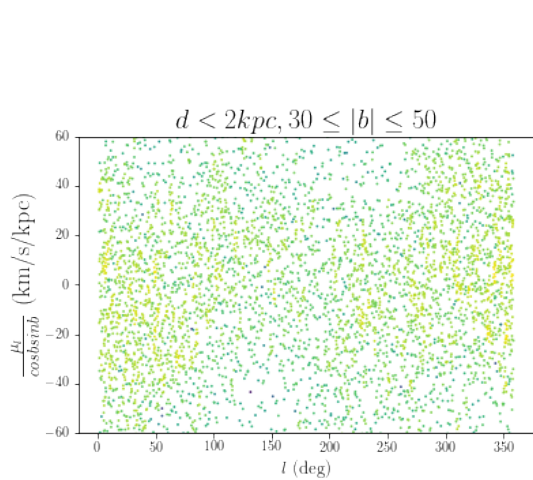


**Figure 11:** Longitudinal profiles of  $\mu_b/\cos b \sin b$  for stars with  $d < 2\text{kpc}$ ,  $30^\circ < |b| < 50^\circ$  from simulation. All the individual data points are shown in this plot. There is no predicted double sinusoidal dependency on  $l$  until we use binned medians.

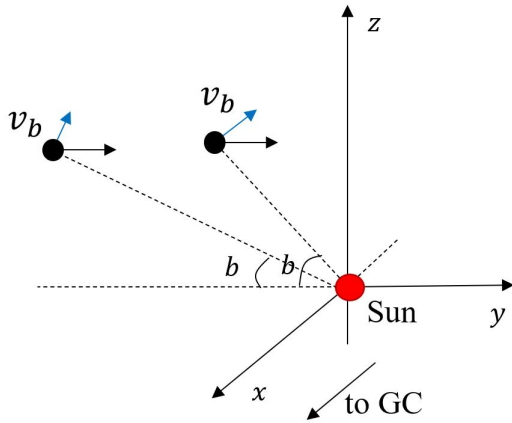


**Figure 12:** The change in latitude  $b$  and  $v_b$  with respect to the Sun for a star in a circular orbit at some vertical height over the MW mid-plane. In this idealized picture, the absolute height of the star does not change because  $v_z$  is set to 0, but its Galactic latitude changes as it approaches or moves away from the Sun.

Because the derivation of Oort constants assumes that stars are close to the MW mid-plane, the discussions on  $\mu_l$  and  $v_{los}$  are more prevalent than the motion approaching or leaving the MW mid-plane. In fact,  $\mu_b$ , the proper motion in the latitudinal direction is also a kinematic tracer of the MW differential rotation. In Fig 12, let's look at a star at some vertical distance from the MW mid-plane and on a hypothetical circular orbit with a constant  $v_\phi$  and  $v_z = 0$ .<sup>1</sup> As this star rotates around the GC at a different  $v_\phi$  than the Sun, its relative position with respect to the Sun changes, so it appears to approach or move away from the Sun while maintaining its absolute height. The angle between the line-of-sight and the horizontal plane parallel to the Milky Way mid plane, which is just the Galactic latitude  $b$ , results in a  $\sin b$  velocity component in the Galactic latitude  $b$  direction perpendicular to the line-of-sight,  $v_b$ . As illustrated in Fig 12, this  $b$  angle varies when the star moves closer or away from the sun, so does  $v_b$ . Therefore,  $\mu_b = \frac{v_b}{d}$  is also a tracer for the stellar in-plane motion. Its dependency

<sup>1</sup> Such an orbital configuration is not valid. We only use it for the purpose of demonstrating the connection between  $\mu_b$  and differential  $v_\phi$  around the Milky Way center.

on  $l$  can be used to derive Oort constants and study the differential rotation of the Milky Way. This component,  $v_b$ , is larger for stars with higher  $b$  because of the  $\sin b$  component. Thus, in our simulation, we look at  $\mu_b$  of stars with mid range  $b$  values. However, for stars with very high  $|b|$ , that is away from the disc in the vertical direction, their orbits are rather non-circular due to the potential perturbation in the vertical direction. These stars tend to have larger vertical velocities, which can give a more dominant contribution to  $\mu_b$  than the effect coming from differential rotation discussed above.

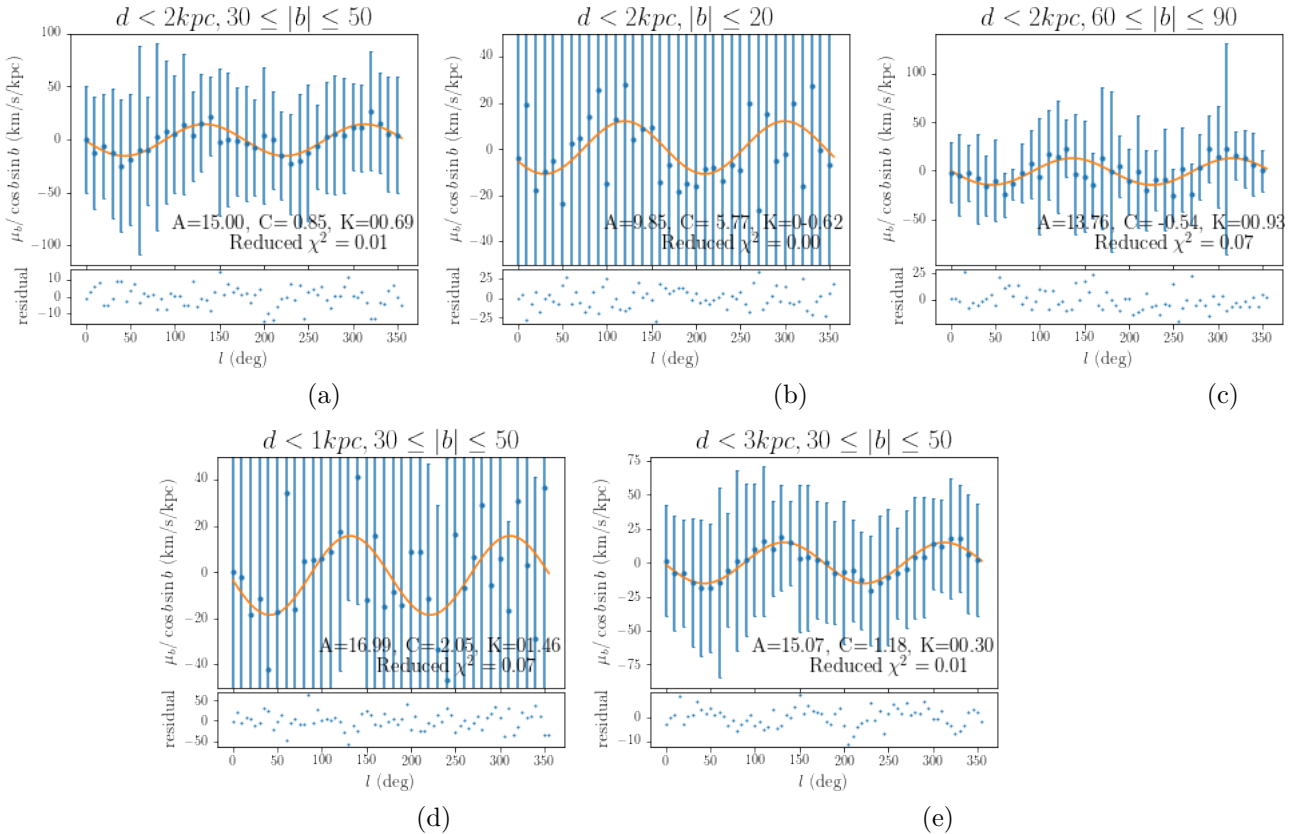


**Figure 13:** The function of binned median  $\mu_b / \cos b \sin b$  over  $l$  for stars with different latitude and distance cut-off. On the first row  $d < 2\text{kpc}$  and (b)  $|b| \leq 20^\circ$ , (a)  $30^\circ < |b| \leq 50^\circ$ , and (c)  $60^\circ < |b| \leq 90^\circ$ . The second row keeps  $30^\circ < |b| \leq 50^\circ$ , while in (d)  $d \leq 1\text{kpc}$ , (e)  $d \leq 3\text{kpc}$ .

In Fig 13, compared to the stars closer to the MW disk ( $|b| < 20^\circ$ ) or those that are much farther away from the MW disk ( $|b| > 60^\circ$ ), stars with  $|b|$  between  $30^\circ$  and  $50^\circ$  yield the most noticeable double sinusoidal variation with  $l$ . In the residuals profiles, the residual for the group with  $30^\circ < |b| < 50^\circ$  distribute randomly over the smallest range compared to the other two groups. This suggests that the group with  $30^\circ < |b| < 50^\circ$  gives the most satisfactory fit to the model predicted by Eq. 13.

On the other hand, in the second row of Fig 13, for larger spatial coverage,  $d < 4\text{kpc}$ , binned median of  $\mu_b/\cos b \sin b$  shows a more evident double sinusoidal function than stars within 2kpc and 1kpc. The residual profile (bottom panels) suggests that the dispersion about the medians is the smallest when all the samples in a larger region around the Sun are included. This is likely due to the fact that a larger sample size, the binned medians are less subjective to any extreme individual values. However, the trade-off for including more samples is applying the first-order Taylor expansion in a much larger region than Sun vicinity.

### 3.2. The effect of radial and vertical velocity values on $\mu_l$ , $v_{los}$ , $\mu_b$

In Fig. 14, we include the longitudinal profiles  $\mu_l/\cos b$ ,  $v_{los}/d$  and binned median of  $\mu_b/\cos b \sin b$  under different constraints on radial velocity  $v_r$  and vertical velocity  $v_z$ : 1) no constraints on  $v_r$  or  $v_z$  2) artificially setting  $v_r = 0$  and 3) artificially setting  $v_z = 0$ . The result shows the spread in  $\mu_l$  is due to the variation of  $v_r$ . Both  $v_r$  and  $v_z$  make contributions to the scattering in  $v_{los}/d$ . When  $v_r$  is set to 0, the scattering around the central double sine curve is smaller as the brighter color indicates a higher density. Meanwhile, the contribution to the scatter in  $v_{los}/d$  by  $v_z$  is more significant. The difference of the binned median of  $\mu_b$  under three velocity profiles shows the deviations from the double sine function described by the Oort constants is attributed to the non-zero vertical velocity stars, consistent with the discussion in section 3.1.4.

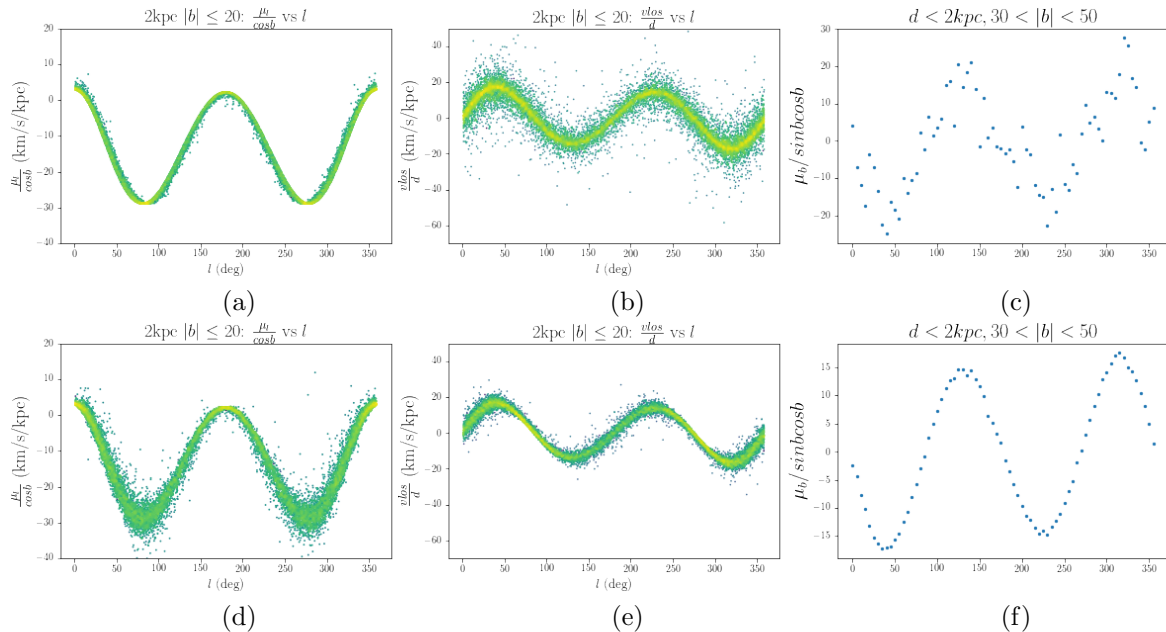


**Figure 14:** The longitudinal profiles of  $\mu_l/\cos b$ ,  $v_{los}/d$  and binned median of  $\frac{\mu_b}{\cos b}$  as a function of  $l$  and under two different velocity profiles. On the top row,  $v_r = 0$ , while on the bottom row,  $v_z = 0$ .

### 3.3. *Gaia DR2 observational data*

#### 3.3.1. *Gaia DR2: using the filtering criteria from literature*

We now present results using *Gaia* DR2 data described in Section 2. In Fig 15, we show the  $\Delta\mu_l$  as a function of  $l$  in the region within  $d < 500\text{pc}$  and  $|b| < 20^\circ$  for stellar populations with  $G_{BP} - G_{RP} - E(BP - RP) < 0.8$ ,  $0.8 \sim 1, 2$ ,  $1.2 \sim 1.6$ ,  $1.6 \sim 2.0$ ,  $2.0 \sim 2.4$  and  $\geq 2.4$ . At least for the first three stellar population based on color, the binned medians of  $\Delta\mu_l$  vs  $l$  fits Eq. 12. The deviation from the double cosine function is larger for redder stellar populations as we move across the panels from (a) to (d) in Fig 15. This is consistent with the fact that redder stars are kinematically older and reside in hotter and more perturbate thus less circular orbits. We also notice that there is a population of stars concentrated at  $l = 280^\circ$  and  $\mu_l$  around 20 km/s/kpc.

Similar to  $\mu_l$ ,  $v_{los}$  for the two bluest stellar population calculated from the radial velocity data in DR2 are also well described by the double sine function predicted by the Oort constants (Fig 16). Despite that the radial velocity data entry is not available for all the stars in DR2, the two bluest stellar populations in Fig 16 show that  $v_{los}$  can be used to derive the Oort constants. Table 2 shows the estimated peculiar motion  $(u_0, v_0)$  from fitting  $\mu_l$  in Fig 15 by maximum likelihood estimation.

**Table 2:** The value of the solar peculiar motion  $(u_0, v_0, w_0)$  such that the binned medians of  $\Delta\mu_l$  in Fig 15 fit to  $A \cos(2l) + C \sin(2l) + B$ . For  $w_0$ , we adopt the value from Schönrich et al. (2010),  $w_0 = 7.25\text{km/s}$  for all six groups.

$BP - RP - E(BP - RP)$	$u_0(\text{km s}^{-1})$	$v_0(\text{km s}^{-1})$
< 0.8	11.65	16.25
$\geq 0.8$ and $< 1.2$	11.10	18.61
$\geq 1.2$ and $< 1.6$	10.88	19.24
$\geq 1.6$ and $< 2.0$	10.46	18.70
$\geq 2.0$ and $< 2.4$	10.50	18.56
$\geq 2.4$	10.69	19.31

While the  $l$  dependencies of  $\mu_l$  and  $v_{los}$  for the stars in DR2 are consistent with the equations of the Oort constants,  $\mu_b$  for stars in the solar vicinity and intermediate  $|b|$  range is a less accurate tracer to derive the Oort constants. Despite the binned medians of  $\Delta\mu_b$  generally follow predicted the double sinusoidal curve except in the reddest population in Fig. 17f, the dispersion in  $\Delta\mu_b$  is much larger than those in  $\Delta\mu_b$  and  $\Delta v_{los}$  as evidenced by the error bars. This larger scatter in  $\Delta\mu_b$  is not due to a smaller sample size like in our simulation, but the significant intrinsic vertical motions of the stars. This suggests that  $\mu_b$  is a less reliable tracer for deriving the Oort constants.

Table 3 lists the values of the Oort Constants and their uncertainties estimated from the results in Fig 15, 16 and 17 using MCMC.  $\Delta v_{los}$  is included in the two bluest group, while  $\Delta\mu_b$  is included in the likelihood function for all but the reddest group.

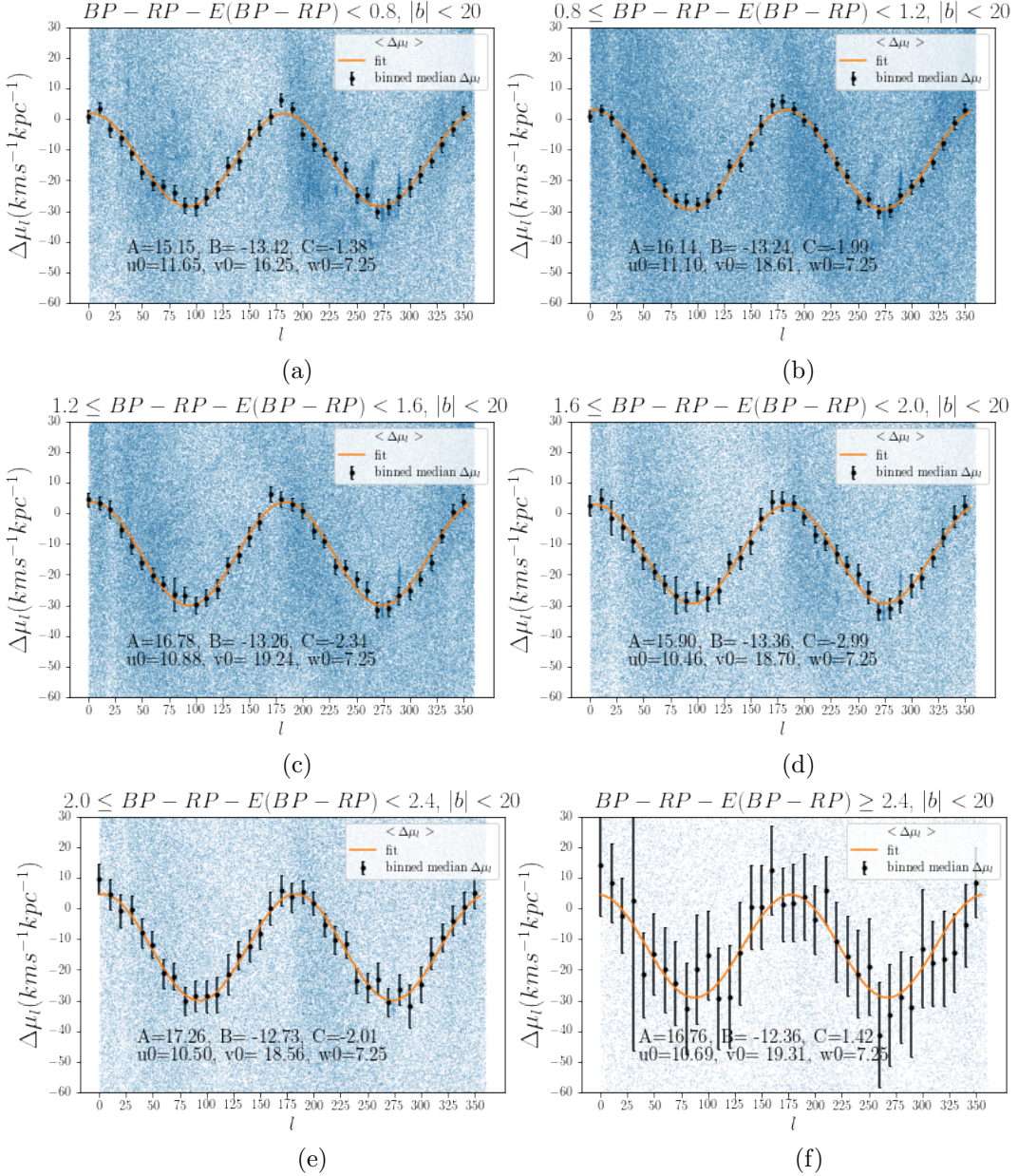


**Figure 15:**  $\Delta\mu_l$  as a function of  $l$  for stars with  $d < 500$  pc and  $|b| < 20^\circ$  divided into groups with  $G_{BP} - G_{RP} - E(BP - RP) < 0.8, 0.8 \sim 1, 2, 1.2 \sim 1, 6, 1.6 \sim 2.0, 2.0 \sim 2.4$  and  $\geq 2.4$ .

Fig 18 shows the parameter MCMC fit results for the bluest  $BP - RP - (E(BP - RP)) < 0.8$  stellar group.

### 3.3.2. Applying filtering criteria based on Simulation to Gaia DR2

In Section 3.1, we show that by limiting the galactic distance to less than 1 kpc and attitude to less than  $20^\circ$ ,  $\mu_l$  and  $v_{los}$  are good tracers for deriving the Oort constants. In Fig. 19, we expand the distance cut off on DR2 data to 1 kpc. The corresponded

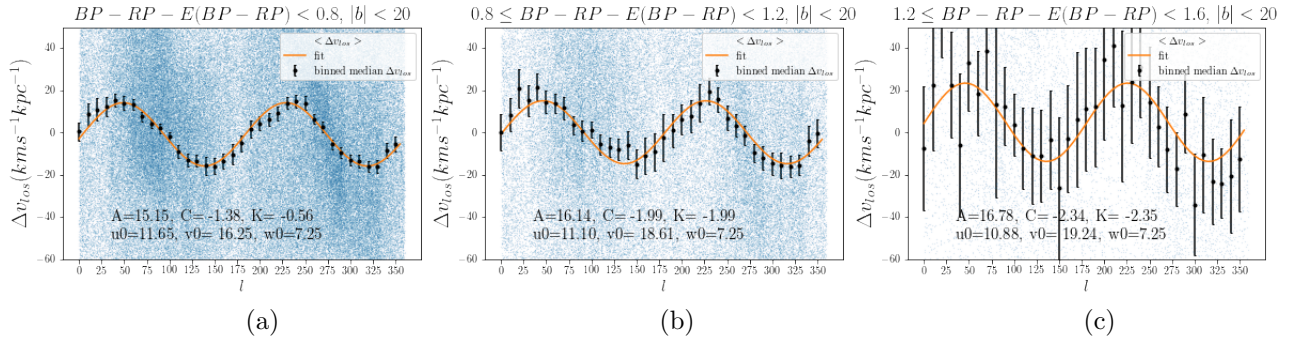


**Figure 16:**  $\Delta v_{los}$  as a function of  $l$  for stars with  $d < 500$  pc and  $|b| < 20^\circ$  divided into groups with  $G_{BP} - G_{RP} - E(BP - RP) < 0.8$ ,  $0.8 \sim 1.2$ ,  $1.2 \sim 1.6$ , and  $1.6 \sim 2.0$ .

**Table 3:** The values of the Oort Constants and their uncertainties estimated from the results in Fig 15, 16 and 17 using MCMC. For the two bluest groups (top two rows),  $\Delta\mu_l$ ,  $\Delta\mu_b$  and  $\Delta v_{los}$  are considered together in MCMC. Only  $\Delta\mu_l$  and  $\Delta\mu_b$  are included for the next three color groups. And for the last population in the table, the reddest population, only  $\mu_l$  is considered, thus, the value of  $K$  is not estimated.

$BP - RP - E(BP - RP)$	$A(km/s/kpc)$	$B(km/s/kpc)$	$C(km/s/kpc)$	$K(km/s/kpc)$
< 0.8	$15.00 \pm 0.24$	$-13.32 \pm 0.22$	$-1.66 \pm 0.31$	$-0.93 \pm 0.36$
$\geq 0.8$ and $< 1.2$	$15.93 \pm 0.31$	$-13.18 \pm 0.24$	$-1.96 \pm 0.26$	$-0.67 \pm 0.43$
$\geq 1.2$ and $< 1.6$	$16.78 \pm 0.40$	$-13.35 \pm 0.28$	$-2.32 \pm 0.33$	$-2.18 \pm 1.04$
$\geq 1.6$ and $< 2.0$	$15.83 \pm 0.44$	$-13.36 \pm 0.38$	$-2.70 \pm 0.46$	$-2.09 \pm 1.09$
$\geq 2.0$ and $< 2.4$	$17.15 \pm 0.83$	$-12.88 \pm 0.55$	$-2.00 \pm 0.78$	$-3.20 \pm 1.49$
$\geq 2.4$	$17.02 \pm 2.12$	$-12.64 \pm 1.43$	$-0.94 \pm 2.16$	NA

fitted Oort constants are:  $A = 16.04 \pm 0.09$ ,  $B = -13.62 \pm 0.07$ ,  $C = -1.88 \pm 0.10$ ,  $K = -1.85 \pm 0.21$  km/s/kpc. It is shown in these plots that at 1kpc, for all three motions, the deviation from the predicted double sinusoidal models are larger than at 500 pc. Still, the fitted Oort constants are relatively in agreement with those in Table 3. This implies distance is a less strict cut-off criterion than the restriction that the Taylor expansion in Eq. 6 imply.

#### 4. DISCUSSION

For our test particle simulations, based on the comparison of the longitudinal profiles of  $\mu_l$  and  $v_{los}$  under different Galactic distance and latitudinal restrictions in Section 3.1, we choose  $d < 1$  kpc and  $|b| < 20^\circ$  as the sampling criteria in extracting the longitudinal profiles of  $\mu_l/\cos b$  and  $v_{los}/d$ . And we ignore  $\mu_b/\cos b \sin b$  in deriving the Oort constants because its much larger deviation compared to  $\mu_l/\cos b$  and  $v_{los}/d$ . With MCMC that includes only  $\mu_l/\cos b$  and  $v_{los}/d$ , we determine the best-fitting Oort constants and their uncertainties as:  $A = 15.62 \pm 0.34$ ,  $B = -12.78 \pm 0.31$ ,  $C = 1.31 \pm 0.40$ ,  $K = 0.24 \pm 1.09$ , in the unit of km/s/kpc.

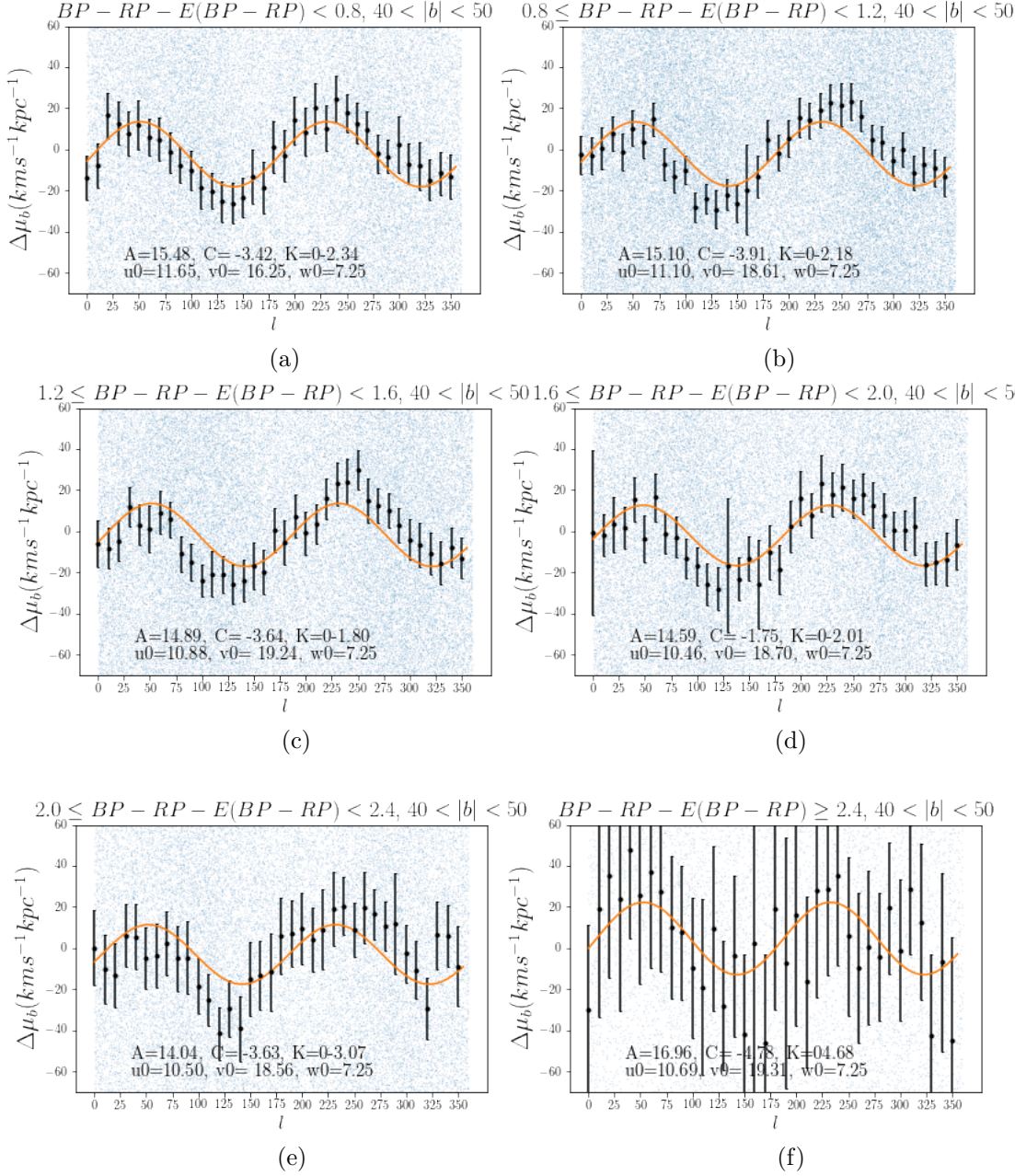


**Figure 17:**  $\Delta\mu_b$  as a function of  $l$  for stars with  $d < 500$  pc and  $40^\circ < |b| < 50^\circ$  divided into groups with  $G_{BP} - G_{RP} - E(BP - RP) < 0.8, 0.8 \sim 1.2, 1.2 \sim 1.6$ , and  $2.0 \sim 2.4$ .

In our simulation, the theoretical slope of rotation curve under MWpotential2014 is  $-(A+B) = \frac{dv_T}{dR} = -2.90$  km/s/kpc. We also know from Eq. 1 that  $A-B = \frac{v_{circ\odot}}{R_\odot} = \frac{240}{8.3}$  km/s/kpc. Therefore, the theoretical values for A and B are:  $A = 15.84, B = -12.94$  km/s/kpc. The values obtained in our simulation are in good agreement with these values.

Meanwhile, for *Gaia* DR2 data, from Table. 3, we see that the Oort constants vary among different color groups. For the two reddest population with  $BP - RP -$

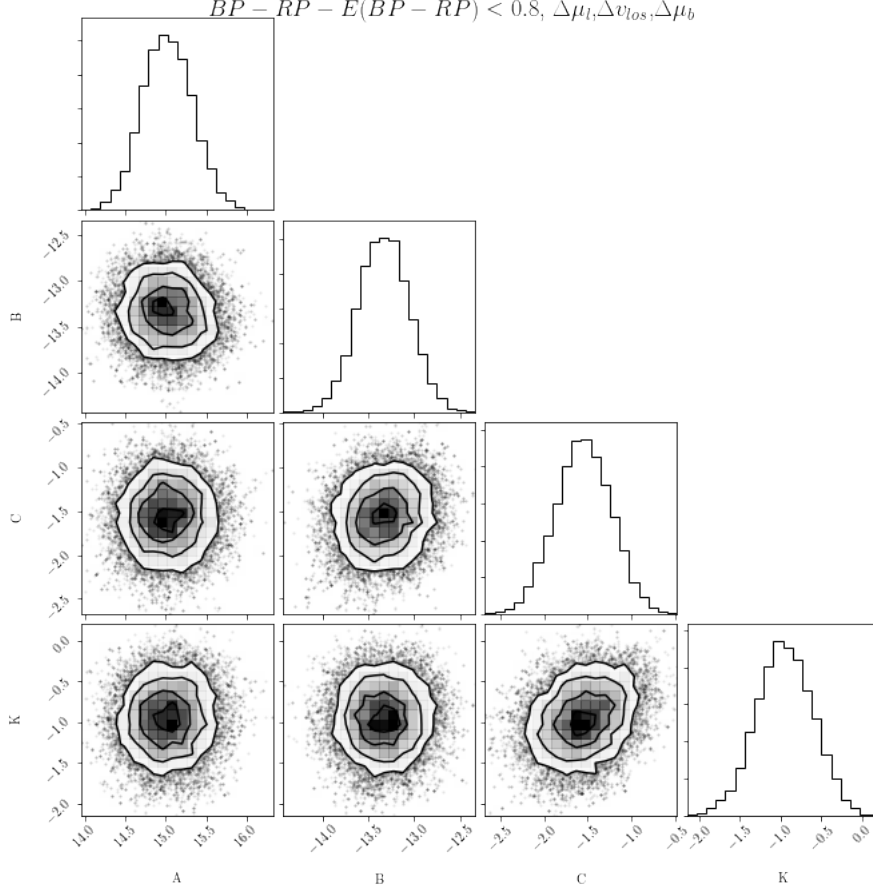


**Figure 18:** Fit result of the Oort constants (A, B, C, K) for  $BP - RP - E(BPRP) < 0.8$  using  $\Delta\mu_l$ ,  $\Delta\mu_b$  and  $\Delta v_{los}$ . Similar plots have been made for all the other color groups.

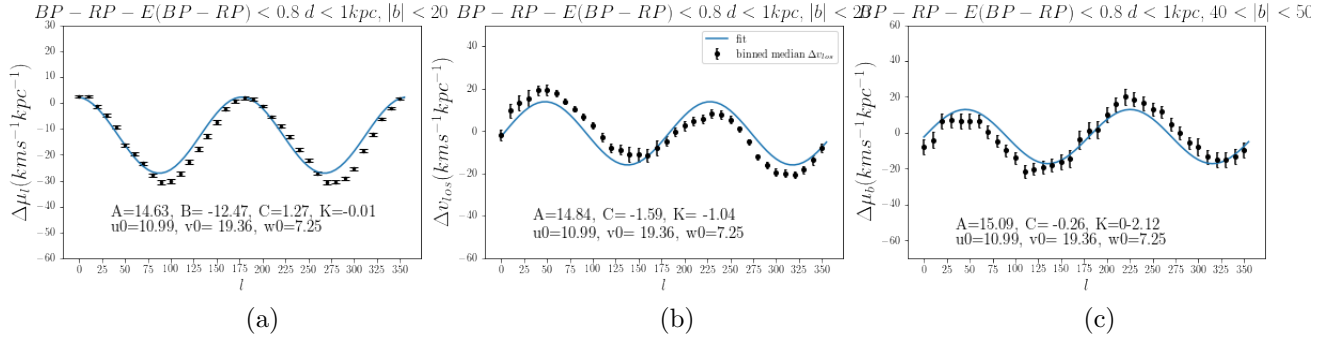


**Figure 19:** The longitudinal profiles of  $\Delta\mu_l$ ,  $\Delta v_{los}$  and  $\Delta\mu_b$  for stars with  $d < 1 \text{ kpc}$  and  $G_{BP} - G_{RP} - E(BP\_RP) < 0.8$  in Gaia DR2. The scattered individual data points are not included because the sample sizes are very large.

$E(BP - RP) > 2.0$ , the estimated value of  $A$  and  $B$  differ significantly from the theoretical value above. The uncertainties in the parameters are also larger with

these kinematically older groups with larger velocity dispersion. It also seems the values of  $A$  and  $B$  do not have strong and consistent dependency on the stellar age.

Thus, we conclude that the  $\Delta\mu_l$  and  $\Delta v_{los}$  of the two bluest stellar population in *Gaia* DR2 data,  $BP - RP - E(BP - RP) < 1.2$ , in 500pc from the Sun and latitude of less than  $20^\circ$  are relatively very accurate tracers to derive the Oort constants. This data filtering criteria yields:

$$A = 15.52 \pm 0.22, B = -13.33 \pm 0.17, C = -1.88 \pm 0.08, K = -1.86 \pm 0.19 \text{ km/s/kpc.} \quad (20)$$

And the estimated solar peculiar motion about LSR ( $10.99, 19.36, 7.25$ ) km/s. This peculiar motion is in good measurement to the result of the  $BP - RP - E(BP - Rp) < 0.8$  group in [Li et al. \(2019\)](#).

The measurements for  $A$  and  $B$  from our simulations and analysis on *Gaia* DR2 are in good agreement with each other and those obtained by [Li et al. \(2019\)](#) and [Bovy \(2017\)](#). The local gradient of the rotation curve is given by  $\frac{dv_\phi}{dR} = -(A + B)$ . According to our results from both simulation and *Gaia* DR2, the slope of rotation curve at  $R_\odot$  is negative. It indicates the circular velocity decreases in the solar vicinity, which is in agreement with the rotation curve in Fig 1.

Recall in the Introduction, we mentioned that the mean offset value  $K$  describes the divergence in the local velocity field.  $K$  from simulation is not significantly different from 0, confirming that Milky Way simulated from quasi-isothermal distribution is axisymmetric. On the other hand, the non-zero mean offset derived from *Gaia* DR2 shows the motions in our actual Milky Way is non-axisymmetric. The local radial velocity gradient is related to the Oort constants  $C$  and  $K$  by  $\frac{\partial v_R}{\partial R} = K + C$ . The value in Eq. 20 suggest this gradient is  $-3.74 \pm 0.21$ . Our measurement of  $C$  and  $K$  are slightly more positive than those in [Bovy 2017](#) but in agreement with [Li et al. 2019](#) within uncertainty.

Our result on  $\mu_b$  from simulation and *Gaia* DR2 do not agree with [Li et al. 2019](#) very well. However, based on the results from our simulation, it is expected that the dispersion of  $\mu_b$  and its deviation from the predicted function are larger compared to  $\mu_l$  and  $\mu_b$ . The comparison of the  $v_\phi$  vs  $v_r$  phase plot between stars with  $|b| < 20^\circ$  and  $40^\circ < |b| < 50^\circ$  in Appendix Fig 23 shows that the radial velocities about the GC for the stars with  $40^\circ < |b| < 50^\circ$  are distributed over a larger non-zero range than the stars with  $|b| < 20^\circ$ . This suggests that the stars which are used to derive Oort constants from their proper motions in the latitudinal direction reside in more non-circular orbits. Because the assumption for Oort constants is circular orbital motion, more consideration is needed when using  $\mu_b$  to derive the Oort constants. In Section 3.2, we has also showed that  $\mu_b$  has strong double sinusoidal dependency on  $l$  as predicted by Eq. 12 when the stars are in purely circular motions parallel to the MW mid-plane ( $v_{\pm 0}$  and  $v_z = 0$ ).

## 5. CONCLUSION

The Oort constants give a predicted model for the rotation around the Sun. At the same time, they are connected to the rotation kinematics of the larger Milky Way by the slope of rotation curve. We review and investigate the methods to derive the Oort constants from test particle simulation and *Gaia* DR2 observational data. Especially, we examine the choice on galactic latitude constraints. We find that for the idealized simulation under axisymmetric potential assumption, it is necessary to limit the distance within 1kpc and latitude range  $|b| < 20^\circ$  to achieve a good fit based on the longitudinal profile of  $\mu_l$  and  $v_{los}$ .

In analyzing *Gaia* DR2 observational data, the Oort constants are affected by stellar age.  $\Delta\mu_l$  and  $\Delta v_{los}$  of the relatively bluer stars are more reliable tracers to derive the Oort constants. Although theoretically latitudinal proper motion reflects the in-plane local rotation that the Oort constants describes, in both our idealized simulations and the DR2 observation data,  $\mu_b$  is not a reliable tracer to derive the Oort constants from local rotation kinematics compared to  $\Delta\mu_l$  and  $\Delta v_{los}$ . The main reason is that stars have intrinsic vertical velocity due to vertical potential perturbation that dominate the effect we expect from the differential rotation in the MW (See Fig. 12). Constraining DR2 samples to within 500 pc from the Sun and lower than  $|20^\circ$  latitude gives a fair approximation to the 2D solar vicinity region that the theoretical Oort constants derivation assumes. Using  $\Delta\mu_l$  and  $\Delta v_{los}$ , we estimate the Oort constants as  $A = 15.52 \pm 0.22$ ,  $B = -13.33 \pm 0.17$ ,  $C = -1.88 \pm 0.08$ , and  $K = -1.86 \pm 0.19$  km/s/kpc.

In Appendix 6.1, we address that the lack of extinction and color excess data prevents us from using similar procedures to analyze EDR3. These data are expected to be published in DR3 in the first half of 2022 (Gaia Collaboration et al. 2020). The result from this work provides guidance for deriving the Oort constants from DR3 once these data are available.

## ACKNOWLEDGMENTS

This work has made use of data from the European Space Agency (ESA) mission *Gaia* (<https://www.cosmos.esa.int/gaia>), processed by the *Gaia* Data Processing and Analysis Consortium (DPAC, <https://www.cosmos.esa.int/web/gaia/dpac/consortium>). Funding for the DPAC has been provided by national institutions, in particular the institutions participating in the *Gaia* Multilateral Agreement.

I would like to acknowledge the tremendous opportunity to do this work offered by Dr.Zhaoyu Li and Dr.Juntai Shen from Shanghai Jiaotong University, as well as Prof. Karen Masters, and their continuous supports throughout the project.

*Software:* Astropy (Astropy Collaboration et al. 2013, 2018), galpy (Bovy 2015), emcee (Foreman-Mackey et al. 2013) .

## REFERENCES

- |   |  |
|---|--|
| Astropy Collaboration, Robitaille, T. P.,<br>Tollerud, E. J., et al. 2013, A&A, 558,<br>A33, doi: <a href="https://doi.org/10.1051/0004-6361/201322068">10.1051/0004-6361/201322068</a> | Astropy Collaboration, Price-Whelan,<br>A. M., SipHocz, B. M., et al. 2018, aj,<br>156, 123,<br>doi: <a href="https://doi.org/10.3847/1538-3881/aabc4f">10.3847/1538-3881/aabc4f</a> |
|---|--|

- Binney, J. 2010, MNRAS, 401, 2318,  
doi: [10.1111/j.1365-2966.2009.15845.x](https://doi.org/10.1111/j.1365-2966.2009.15845.x)
- Binney, J., & Merrifield, M. 1998,  
Galactic Astronomy
- Bovy, J. 2015, ApJS, 216, 29,  
doi: [10.1088/0067-0049/216/2/29](https://doi.org/10.1088/0067-0049/216/2/29)
- . 2017, MNRAS, 468, L63,  
doi: [10.1093/mnrasl/slx027](https://doi.org/10.1093/mnrasl/slx027)
- Eilers, A.-C., Hogg, D. W., Rix, H.-W., &  
Ness, M. K. 2019, ApJ, 871, 120,  
doi: [10.3847/1538-4357/aaf648](https://doi.org/10.3847/1538-4357/aaf648)
- Feast, M., & Whitelock, P. 1997, MNRAS,  
291, 683, doi: [10.1093/mnras/291.4.683](https://doi.org/10.1093/mnras/291.4.683)
- Foreman-Mackey, D., Hogg, D. W., Lang,  
D., & Goodman, J. 2013, PASP, 125,  
306, doi: [10.1086/670067](https://doi.org/10.1086/670067)
- Gaia Collaboration, Brown, A. G. A.,  
Vallenari, A., et al. 2020, arXiv  
e-prints, arXiv:2012.01533.  
<https://arxiv.org/abs/2012.01533>
- Gaia Collaboration, Prusti, T., de  
Bruijne, J. H. J., et al. 2016, A&A, 595,  
A1, doi: [10.1051/0004-6361/201629272](https://doi.org/10.1051/0004-6361/201629272)
- Gaia Collaboration, Brown, A. G. A.,  
Vallenari, A., et al. 2018, A&A, 616,  
A1, doi: [10.1051/0004-6361/201833051](https://doi.org/10.1051/0004-6361/201833051)
- Green, G. 2018, The Journal of Open  
Source Software, 3, 695,  
doi: [10.21105/joss.00695](https://doi.org/10.21105/joss.00695)
- Joy, A. H. 1939, ApJ, 89, 356,  
doi: [10.1086/144060](https://doi.org/10.1086/144060)
- Kerr, F. J., & Lynden-Bell, D. 1986,  
MNRAS, 221, 1023,  
doi: [10.1093/mnras/221.4.1023](https://doi.org/10.1093/mnras/221.4.1023)
- Kuijken, K., & Tremaine, S. 1994, ApJ,  
421, 178, doi: [10.1086/173635](https://doi.org/10.1086/173635)
- Levine, E. S., Heiles, C., & Blitz, L. 2008,  
ApJ, 679, 1288, doi: [10.1086/587444](https://doi.org/10.1086/587444)
- Li, C., Zhao, G., & Yang, C. 2019, ApJ,  
872, 205,  
doi: [10.3847/1538-4357/ab0104](https://doi.org/10.3847/1538-4357/ab0104)
- Lin, C. C., Yuan, C., & Roberts, W. W.,  
J. 1978, A&A, 69, 181
- Luri, X., Brown, A. G. A., Sarro, L. M.,  
et al. 2018, A&A, 616, A9,  
doi: [10.1051/0004-6361/201832964](https://doi.org/10.1051/0004-6361/201832964)
- Metzger, M. R., Caldwell, J. A. R., &  
Schechter, P. L. 1998, AJ, 115, 635,  
doi: [10.1086/300198](https://doi.org/10.1086/300198)
- Mignard, F. 2000, A&A, 354, 522
- Minchev, I., & Quillen, A. C. 2007,  
MNRAS, 377, 1163,  
doi: [10.1111/j.1365-2966.2007.11661.x](https://doi.org/10.1111/j.1365-2966.2007.11661.x)
- Mróz, P., Udalski, A., Skowron, D. M.,  
et al. 2019, ApJL, 870, L10,  
doi: [10.3847/2041-8213/aaf73f](https://doi.org/10.3847/2041-8213/aaf73f)
- Ogrodnikoff, K. 1932, ZA, 4, 190
- Olling, R. P., & Dehnen, W. 2003, ApJ,  
599, 275, doi: [10.1086/379278](https://doi.org/10.1086/379278)
- Olling, R. P., & Merrifield, M. R. 1998,  
MNRAS, 297, 943,  
doi: [10.1046/j.1365-8711.1998.01577.x](https://doi.org/10.1046/j.1365-8711.1998.01577.x)
- Oort, J. H. 1927, BAN, 3, 275
- Schönrich, R., Binney, J., & Dehnen, W.  
2010, MNRAS, 403, 1829,  
doi: [10.1111/j.1365-2966.2010.16253.x](https://doi.org/10.1111/j.1365-2966.2010.16253.x)
- Sellwood, J. A., & Carlberg, R. G. 2014,  
ApJ, 785, 137,  
doi: [10.1088/0004-637X/785/2/137](https://doi.org/10.1088/0004-637X/785/2/137)
- Siebert, A., Famaey, B., Minchev, I.,  
et al. 2011, MNRAS, 412, 2026,  
doi: [10.1111/j.1365-2966.2010.18037.x](https://doi.org/10.1111/j.1365-2966.2010.18037.x)
- Sofue, Y., & Rubin, V. 2001, ARA&A,  
39, 137,  
doi: [10.1146/annurev.astro.39.1.137](https://doi.org/10.1146/annurev.astro.39.1.137)
- Taylor, M. B. 2005, in Astronomical  
Society of the Pacific Conference Series,  
Vol. 347, Astronomical Data Analysis  
Software and Systems XIV, ed.  
P. Shopbell, M. Britton, & R. Ebert, 29
- Vasiliev, E. 2019, MNRAS, 482, 1525,  
doi: [10.1093/mnras/sty2672](https://doi.org/10.1093/mnras/sty2672)
- Wegg, C., Gerhard, O., & Bieth, M. 2019,  
MNRAS, 485, 3296,  
doi: [10.1093/mnras/stz572](https://doi.org/10.1093/mnras/stz572)

## 6. APPENDIX

### 6.1. EDR3

In December 2020, ESA released the third early intermediate *Gaia* data (EDR3). This version catalogs the positions and proper motions, and other photometric data of 1.8 billion stars, 1.6 billions entries of which are updated from DR2. EDR3 does not contain new radial velocity data. It adopted the 7.2 million data in DR2 after deleting 4000 wrong entries. We considered using the available data in EDR3 to further derive the Oort constants using the same methods for DR2, but because EDR3 deleted several entries from DR2, including color excess and extinction ([Gaia Collaboration et al. 2020](#)), we decided not to apply our analysis on DR2 to EDR3.

Extinction  $A_G$  and color excess  $E(B - V)$  must be considered when making an H-R diagram to reflect the properties of stars accurately, and further grouping stars into different color populations that vary in their kinematic properties. However, spectroscopic data, such as radial velocity, extinction, and color excess are not yet available for the 100 million newly added stars in EDR3. These data are expected to be published in DR3 in the first half of 2022 ([Gaia Collaboration et al. 2020](#)). We use the *DUSTMAP* python library to estimate  $E(B - V)$  in EDR3. The reason for not doing doing a cross-match with DR2 samples is that the new spectroscopic measurements in EDR3 and DR3 use different blue and red photometers than those in DR2. *DUSTMAP* gives a 3D map of interstellar dust reddening probabilistically based on broadband photometric measurement from Pan-STARRS 1, 2MASS, and *Gaia* parallaxes ([Green 2018](#)). Each  $(l, b, d)$  corresponds to a color excess value in the default *bayestar17* module in DUSTMAP. Multiplying color excess by  $R_v = 3.1$  gives us the corresponding extinction. For EDR3, the Galactic coordinates  $(l, b, d)$  are first retrieved from TOPCAT, then used to find  $E(B - V)$  and  $A_G$  in python. Fig 20 shows the H-R diagram after correcting parallax, extinction and color excess as described above. For the purpose of comparison with the H-R diagram of DR2 in Fig. 4, the scale and limits are set to the same as those in Fig. 4. The value of color excess given by *DUSTMAP* is larger compared to the actual measurement in DR2. This means it is not appropriate to use the criteria based on  $BP - RP - E(BP - RP)$  in [Li et al. \(2019\)](#) to divide stellar samples into different color groups.

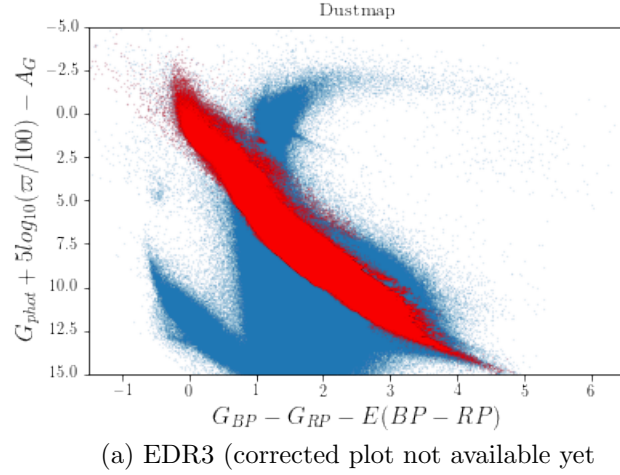


**Figure 20:** The H-R diagram and Main sequence star samples in EDR3 after parallax, extinction and color excess correction interpolated with DUSTMAP. For the purpose of comparison with the H-R diagram of DR2 in Fig. 4, the scale and limits are set to the same as those in Fig. 4.

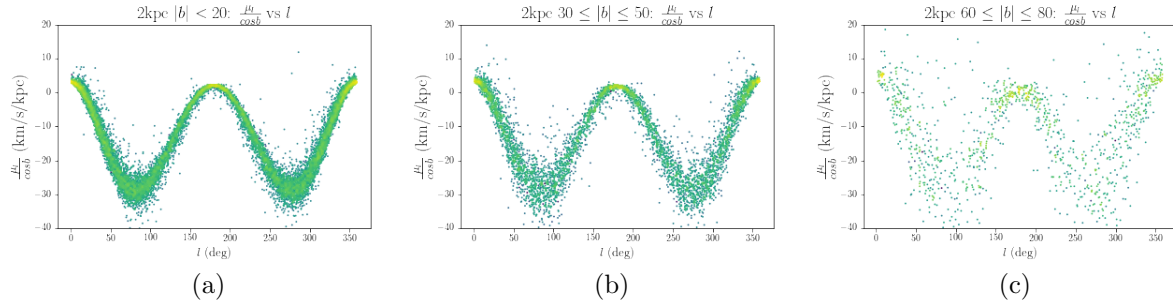


**Figure 21:** The distribution of  $\mu_l / \cos b$  over  $l$  for stars with  $d < 2$ kpc and (b)  $|b| < 20^\circ$ , (b)  $30^\circ \leq |b| \leq 50^\circ$ , and (c)  $60^\circ \leq |b| < 80^\circ$ .

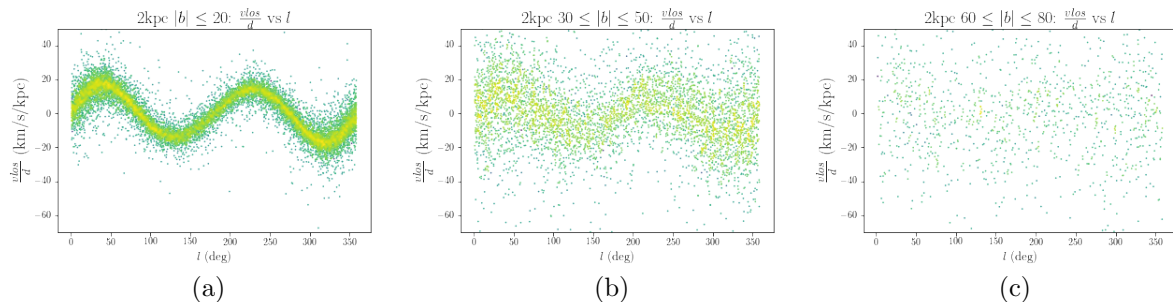


**Figure 22:** The distribution of  $v_{los}/d$  over  $l$  for stars with  $d < 2$ kpc and (a)  $|b| < 20^\circ$ , (b)  $30^\circ \leq |b| \leq 50^\circ$ , and (c)  $60^\circ \leq |b| < 80^\circ$ .

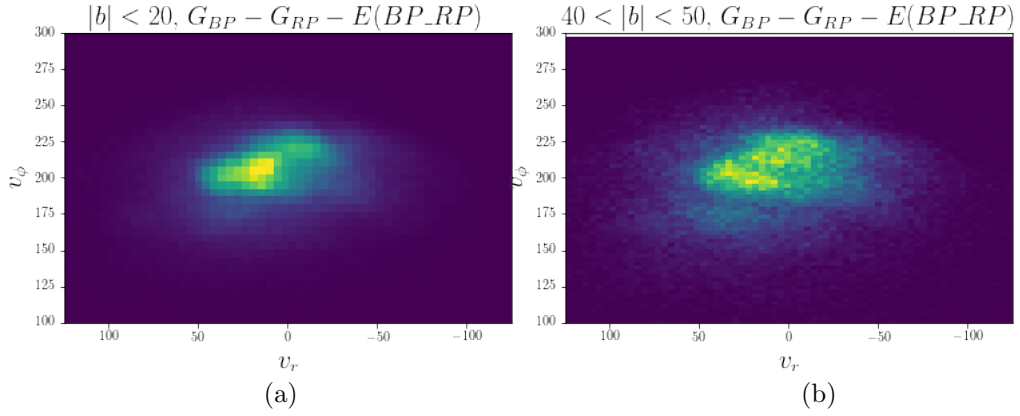


**Figure 23:** *Gaia* DR2: The phase plot of  $v_r$  VS  $v_\phi$  for stars at  $|b| < 20^\circ$  and  $40^\circ < |b| < 50^\circ$  within 500 pc from the Sun. For  $|b| < 20^\circ$ , more data are centered around  $v_\phi - 220$  and  $v_r = 0$ , which resembles circular orbit in the solar vicinity.